Angewandte Chemie
Eine Zeitschrift der Gesellschaft Deutscher Chemiker

Supporting Information

69451 Weinheim, Germany

Internal Dynamics of the Homotrimeric HIV-1 Viral Coat Protein gp41 on Multiple Time Scales**

Nils-Alexander Lakomek, Joshua D. Kaufman, Stephen J. Stahl, John M. Louis,
*Alexander Grishaev, Paul T. Wingfield, and Ad Bax**

anie_201207266_sm_miscellaneous_information.pdf

Table of Contents

1. Sample preparation and characterization

1.1. Protein expression and purification

The expression plasmid HIV-1 gp41$^{1-194}$ corresponding to HXB2 Env residues 512 – 706 was generated by the polymerase chain reaction and cloned into the T7 expression vector pet11a. PCR mutagenesis was used to add an N-terminal methionine and change the Cys residues at position 87 and 93 to Ala. The mutant S192C was synthesized by (DNA 2.0 Inc., USA) and cloned onto pJexpress404 vector. Fermentation of plasmids in (BL21-DE3) cells and labeling with combinations of ^{2}H, ^{15}N and ^{13}C were carried out as described previously.[33] Expressed protein was extracted with SDS and purified by a combination of gel filtration and hydroxyapatite chromatographies. The protein was folded by exchanging SDS for Fos-Choline-12 (DPC - Affymetrix). Protein in 50 mM sodium acetate, pH 4.0, 25 mM KCl, 0.1% (w/v) DPC was concentrated to ~ 10 mg/ml with an Amicon-Ultra 15ml, 30-kD concentrator (EMD Millipore). Samples at pH 7.1 were prepared similarly using a pH 9.0- 9.6 buffer for the folding from SDS followed by gel filtation in 50 mM HEPES, pH 7.1 containing 0.1% DPC.

1.2. Size exclusion chromatography with inline multi-angle light scattering

Molecular masses and hydrodynamic radius R_h values were estimated by analytical **S**ize exclusion chromatography with in-line **M**ultiangle light scattering and integrated QELS (DAWN EOS, Wyatt Technology Inc., Santa Barbara, CA), **R**efractive index (Optilab T-rex, Wyatt Technology Inc.), UV (Waters 2487, Waters Corporation, Milford, MA) detectors (**SMR**) and Astra V (version 5.3.4.20) software. Samples (~ injection volume of 200 µL) were fractionated on a Superdex-75 column (1 x 30 cm, GE Healthcare) in 50 mM sodium acetate buffer, pH 4, 25 mM KCl, 2 mM DPC at a flow rate of 0.5 ml/min at room temperature.

The SMR analysis gives information on the overall mass of the gp41^{194}/DPC complex and distinguishes its protein and detergent mass composition. Peak 1 and peak 2 in Figure S1 match closely to a trimeric and monomeric gp41$^{1-194}$/DPC complex, (see Table S1). Accounting for the dilution that occurs during column fractionation, the concentration of gp41$^{1-194}$ in the peak is estimated at ~5 µM.

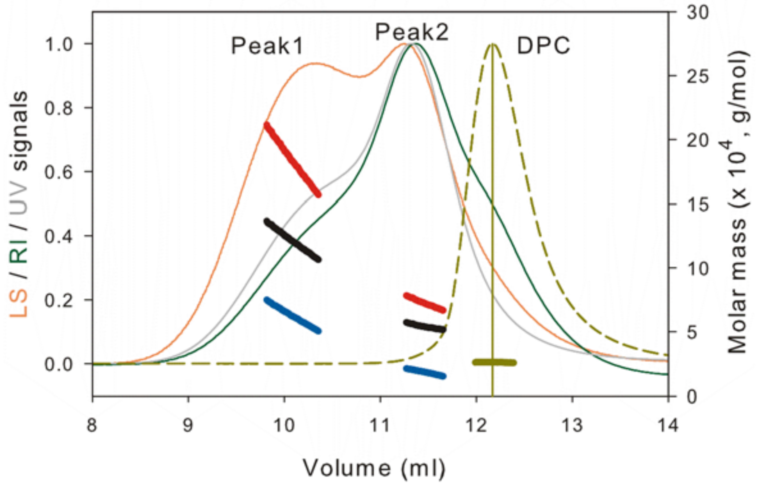

Figure S1. Molecular mass analyses of gp41$^{1-194}$ by **SMR**. Gp41$^{1-194}$ in 50 mM sodium acetate, pH 4, 25 mM KCl and 3 mM DPC was fractionated (150 µg/injection) on a Superdex-75 column at room temperature, equilibrated in the same buffer but with 2 mM DPC. Experimentally determined masses of gp41$^{1\text{-}194}$/DPC complexes and DPC micelle alone are listed in Table S1. Light scattering (LS), refractive index (RI) and absorbance at 280 nm (UV) traces are shown in red, green and gray, respectively. The RI signal attained by fractionating 150 µl DPC (50 mM) is shown as the dashed dark-yellow trace. The gp41/DPC complex masses and their protein and DPC compositions in peak 1 and 2 are shown as thick red, blue and black lines under the peaks, respectively.

Table S1. Experimentally determined molecular masses of gp41$^{1\text{-}194}$/DPC complexes

	Molar Mass (g/mol)			Ratio (protein:DPC)
	Complex (gp41$^{1\text{-}194}$/DPC)	Protein	DPC	
DPC			25980 ± 52[a]	0:74[a]
Peak1	180900 ± 181	61220 ± 122[b]	119700 ± 359	1 trimer:340
Peak 2	72370 ± 72	18310 ± 18	54060 ± 108	1 monomer:154

[a] One DPC micelle corresponds to 74 molecules of DPC

[b] It is noteworthy that the protein mass in peak 1 is about 3 times that of the protein mass in peak 2; the latter corresponds to the monomeric fraction existing at this very dilute concentration.

1.3 Analytical Ultracentrifugation

A Beckman Optima XL-I analytical ultracentrifuge, absorption optics, an An-60 Ti rotor and standard double-sector centerpiece cells were used. Equilibrium measurements were made at 20 °C and the concentration profile was recorded after 20 hours at 18,500 rpm. A baseline was established by over-speeding at 45,000 rpm for 3 hours. The protein was in 50 mM sodium acetate, pH 4.0, 25mM KCl containing ~ 5mM DPC. The mass contribution of the detergent was eliminated using D_2O as described by Noy at al.[34]. The average molecular mass was calculated as 60 kDa assuming a single ideal species model (data not shown). The equilibrium data was, however, best fitted as a monomer-trimer system with a calculated K_d in the low µ-molar range, $K_d = 9.64 \times 10^{11}$ M^{-2}. This is similar to the association of the smaller HIV-1 gp41$^{27\text{-}154}$ construct previously described.[35]

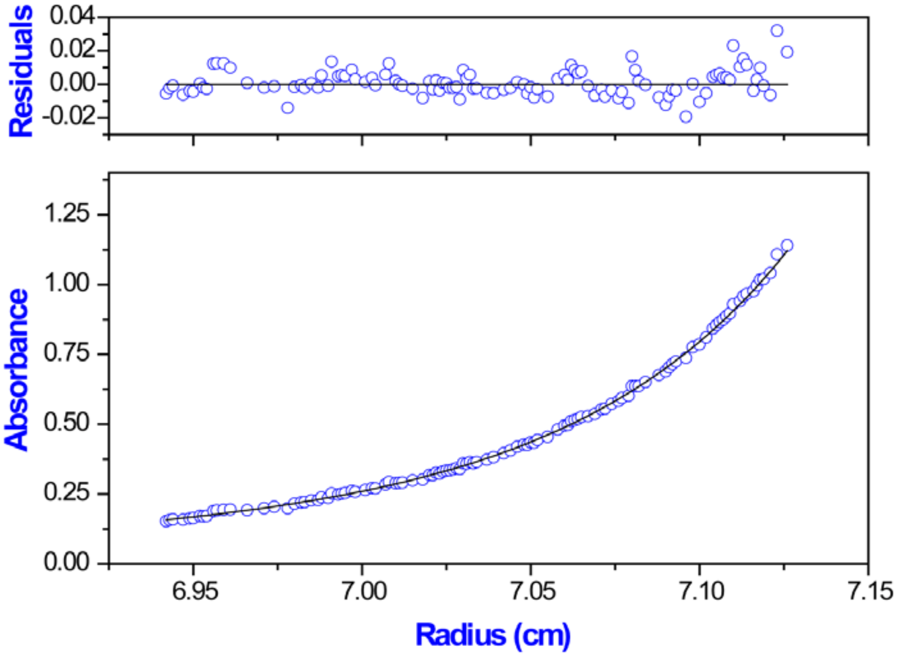

Figure S2. Sedimentation equilibrium of HIV-1 gp41$^{1\text{-}194}$ in 50 mM sodium acetate, pH 4.0, 25 mM KCl, 5 mM DPC. The open circles represent experimental data, and the continuous line a curve fitted using a monomer – trimer association model. The upper panel shows the residuals (difference between the fitted and experimental values) as a function of radial position.

1.4. Circular dichroism

A CD spectrum was recorded on a Jasco J-715 spectropolarimeter using a 0.02-cm path length cell. The protein solution was 0.5 mg/ml in 50 mM sodium acetate, pH 4.0, 25 mM KCl, containing 10 mM n-dodecyl-phosphocholine (DPC). The secondary structure was estimated using the CONTIN program,[36] about 70% of the protein shows helical secondary structure.

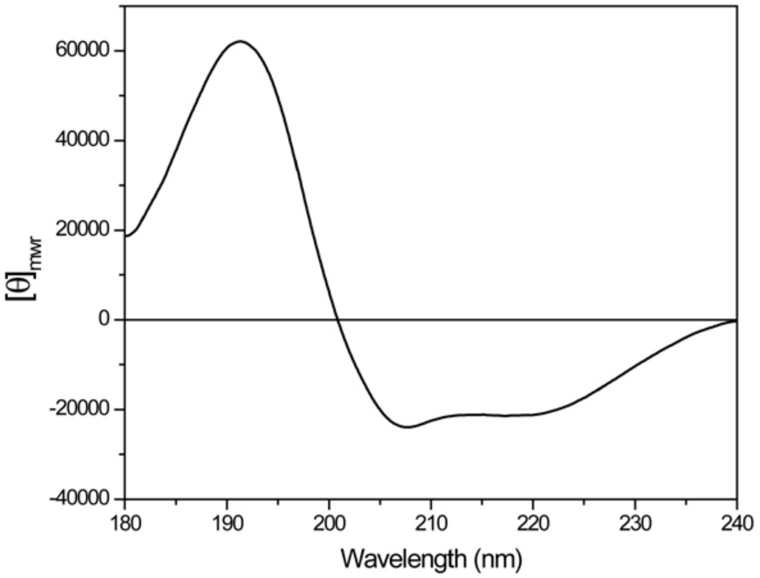

Figure S3. Circular dichroism spectrum of gp41$^{1\text{-}194}$. The protein (0.025 mM) was dissolved in 10 mM DPC, 50 mM sodium acetate, pH 4.0, 25mM KCl, at 20°C. Units of the ordinate [θ_{mwr}] have the dimensions: deg × dmol^{-1} × cm^{-2}.

1.5. SAXS data collection and analysis

Solution X-ray scattering data were acquired at the Beam Line 12-IDC at the Advanced Photon Source (Argonne National Laboratory, Argonne, IL). Data collection was carried out using a mosaic Gold CCD detector positioned in an on-center geometry 3.7 m from the sample capillary, using 18 keV incident radiation, resulting in the observable q-range of 0.01 – 0.23 Å^{-1}. Q-axis mapping was done using a silver behenate standard sample. A total of 20 sequential data frames with exposure times of 1 s were recorded with the samples kept at 25 °C throughout the measurement. In order to prevent radiation damage, volumes of 150 μL of samples and buffers were oscillating during data collection. Individual data frames were masked, corrected for the detector sensitivity, radially integrated and normalized by the corresponding incident beam intensities and sample transmissions. Data were collected from two stock samples, one containing 0.83 mg/mL gp41$^{1\text{-}194}$ and 6 mg/mL DPC, and the other containing 6 mg/mL DPC as a detergent reference sample, and a third sample of the buffer solution. For both DPC-containing samples, data at 50% dilutions were collected as well, to ensure the absence of the inter-particle structure factor effects within the fitted q-range. The final 1D scattering profiles and their uncertainties were calculated as means and standard deviations over the 20 individual frames. The buffer data were then subtracted from the samples and the fraction of unbound DPC (75%, based on the multi-angle light scattering measurements) was then subtracted as well, resulting in the scattering signal corresponding only to the gp41/DPC complexes (Figure S4). Based on the zero-angle scattering intensity values and by reference to measurements on the lysozyme and DPC micelle standard samples of known concentrations, gp41/DPC complex exists in the trimeric state with 300-350 DPC molecules bound to each trimer, corresponding to the fraction of unbound DPC between 78% and 74%, consistent with the MALS data. Due to large size of the gp41/DPC complex relative to the DPC micelle, the scattering signal of gp41/DPC sample is dominated by the former and the impact of the uncertainty in the fraction of the subtracted DPC appears to be negligible (Figure S4). The data between q_{min}=0.016Å^{-1} and q_{max}=0.23Å^{-1} were Fourier-transformed using GNOM software,[37] resulting in a P(r) distribution with a maximum length vector, d_{max}, between 150 and 170 Å (see Figure S5b).

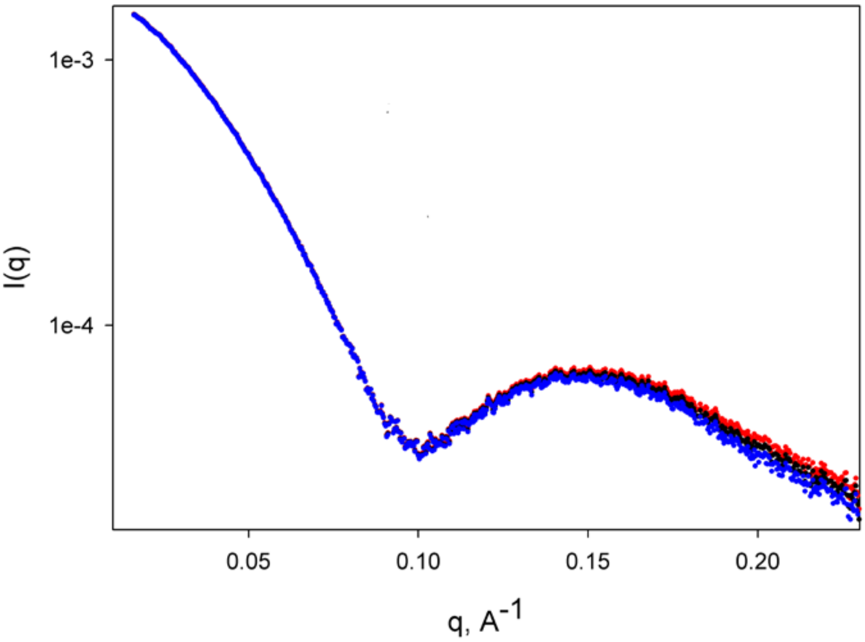

Figure S4. The effect of varying the fraction of subtracted free DPC signal (obtained from a separate DPC-only and buffer sample) from f=0.70 (red line) to f=0.80 (blue line) relative to the target value of f=0.75 (black line) from the experimental gp41/DPC data.

Low-resolution shapes compatible with the gp41/DPC SAXS scattering curve were then determined using DAMMIN software[38]. Since DAMMIN assumes uniform electron density of the reconstructed object, we have limited q_{max} of the fitted data to 0.10 $Å^{-1}$ as higher-q data are increasingly influenced by the inhomogeneity of the electron density of the composite gp41/DPC particle. The resulting low-resolution shapes are fairly compact but asymmetric, with dimensions of 161±6, 45±4 and 67±6 Å (Figure S5c-e), roughly consistent with the two three-helical bundles of the N- and C-terminal parts of the ectodomain, packed side by side in a close to anti-parallel manner, potentially in exchange with a more symmetric object. Note that after averaging the results of multiple DAMMIN runs, the deviation from axial symmetry appears less pronounced than in the individual models, an effect exacerbated by the 5 Å layer padded on its surface for viewing purposes (Fig. S5c-e). Considering the high degree of structural disorder evidenced by the NMR data, the impact of the program's regularizer, and the inhomogeneity of the electron density of the gp41/DPC complex noted above, these shapes are -at best- only approximate representations of the time-averaged geometry of the complex.

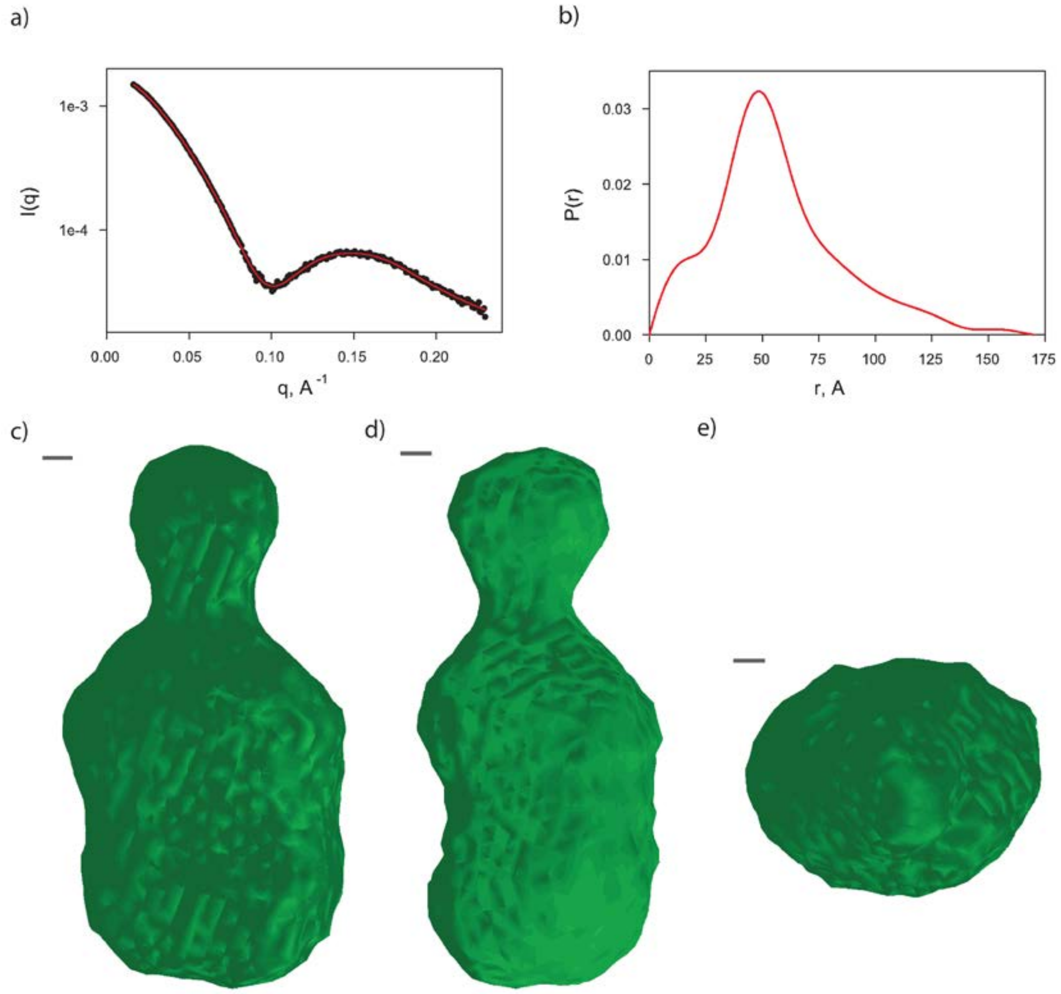

Figure S5. SAXS analysis of $gp41^{1-194}$. (a) SAXS data from the gp41/DPC sample (after subtraction of the free DPC signal) are superimposed onto the Fourier transform of the pairwise distance distribution function, P(r), fitted by the program GNOM [37]. (b) The corresponding P(r) function. (c-e) Orthogonal views of the superimposed low-resolution shapes of the $gp41^{1-194}$/DPC complex obtained from 10 independent runs of the program DAMMIN[38]. The surface of the averaged model has been covered by a 5 Å layer for smoothening its appearance. The lengths of the gray bars in panels c-e correspond to a distance of 10Å.

In order to estimate the magnitude of systematic errors introduced by the neglect of the ensemble averaging, experimental solution scattering data of the gp41/DPC complex also were fitted by structural ensembles of all-atom single models of gp41$^{1\text{-}194}$, consisting of three N-terminal fusion peptides (structure taken from Jaroniec et al.[13] (PDB entry 2ARI)), a flexible linker connecting these FP's to the NHR three-helix bundle taken from the 1AIK structure of Chan et al.,[22] connected by random coil linkers (residues 80-110) to an analogous three-helical bundle arrangement for the CHR region, followed by MPER conformations taken from Sun et al.[16] (PDB entry 2PV6) without forcing a 3-helical arrangement, and an approximate three-helical TM arrangement embedded in a DPC micelle, with two DPC micelles embedding the fusion peptides and C-terminal TM regions. The position of the C-terminal part of gp41 and the corresponding DPC micelle was exhaustively sampled relative to the N-terminal part in a rigid body manner, using an orientational grid with a step of 3° and a translational grid with a step of 3Å. Geometries with clashes and impossible linkages as well as those exhibiting R_{gyr} values exceeding 45 Å (by reference to the measured R_{gyr} of 43Å) were removed, leaving a total of ~2300 candidate structural models. Figure S6 shows the agreement between the experimental fitted data (black dots) and the curve calculated from the best-fitted single model (green line, inter-helical bundle angle of ~50°) with χ=0.55. Predicted scattering functions were also averaged over a 112-member ensemble of the best fitting models selected from the ~2300 candidate structural models (χ<0.7). The best fit between this scattering data and the ensemble is shown as the red line. Comparably close agreement between the fits to a single model and to the ensemble indicates that the impact of structural averaging is limited within the fitted q-range. General agreement between the low-resolution shape fitted by DAMMIN (Figure S5) and the ensemble of best-fitting models shown in the inset of Figure S6 supports this notion. Analogous single-model fits obtained when forcing NHR and CHR regions to adopt the late fusion stage six-helical bundle state of 1AIK structure of Chan et al.[22] can approximately fit the scattering data for q ≤ 0.07/Å, but not for larger q values (Figure S7). A fractional population of this arrangement cannot be excluded, however.

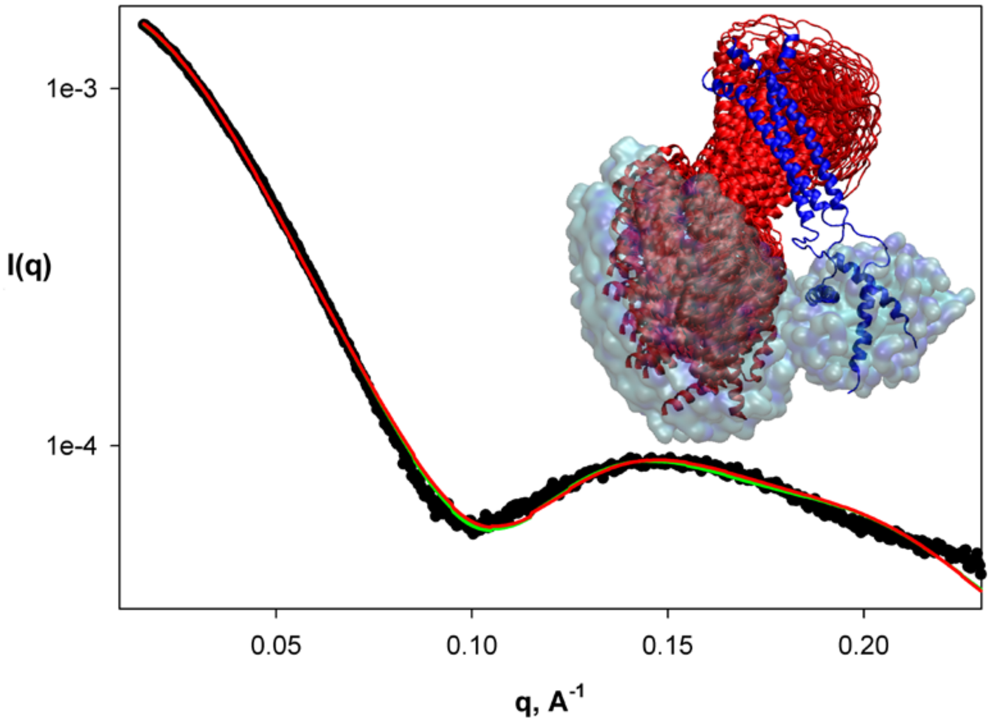

Figure S6. Best fits of the experimental SAXS scattering data for gp41$^{1\text{-}194}$/DPC (black circles) to a single all-atom model (green) and an 112-member ensemble model (red line) where both NHR and CHR are arranged as three-helical bundles, with each helical FP connected by a flexible linker to its NHR, and all three FP's embedded in a single large (190 DPC) micelle. The C-terminal TM domains are arranged as a trimeric cluster, also embedded in a single 190-DPC micelle, with the TM domains linked to the CHR helices by the MPER structures of PDB entry 2PV6. The inset displays the best-fitting gp41/DPC rigid-body ensemble aligned on the N-terminal part (residues 1-80, blue) of the structure, with the flexible C-terminal part of the gp41 ensemble shown in red. The DPC micelles embedding the N-terminal FP and C-terminal TM domains are shown with semi-transparent surfaces.

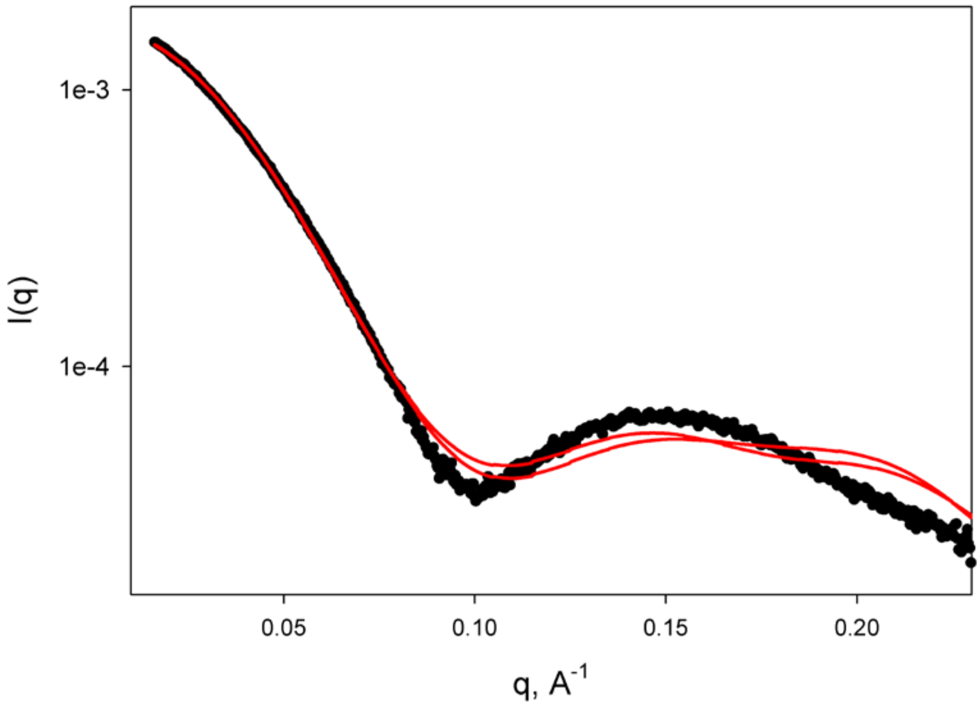

Figure S7. Best fits between the experimental scattering data for gp41/DPC (black circles) and scattering data predicted for late stage fusion models (red lines), optimized in the same manner as the structures of Figure S6, but using a six-helical bundle NHR/CHR arrangement, as observed in the X-ray structure of Chan et al. (PDB entry 1AIK).[22]

2. Additional NMR data

2.1. Comparison of ^{1}H-^{15}N TROSY-HSQC NMR spectra at pH 4 (DPC and DDM) and pH 7.1 (DPC)

^{1}H-^{15}N TROSY-HSQC 600 MHz NMR spectra recorded at acidic and neutral pH and in different detergents, 40 °C, are compared in Figure S8. Two samples contained uniformly ^{2}H,^{15}N,^{13}C-enriched gp41$^{1\text{-}194}$ solubilized in DPC detergent at acidic and neutral pH (0.5 mM gp41$^{1\text{-}194}$, 50 mM sodium acetate, pH 4.0, 25 mM KCl, 330 mM DPC; 0.3 mM protein, 50 mM HEPES, pH 7.1, 200 mM DPC). The third sample contained uniformly ^{2}H,^{15}N,^{13}C-enriched gp41$^{1\text{-}194}$ solubilized in DDM detergent at acidic pH (0.5 mM gp41$^{1\text{-}194}$, 150 mM DDM, 50 mM sodium acetate buffer, pH 4, 100 mM NaCl).

The low pH sample in DPC micelles (red) was highly stable and its spectra were not compromised by amide exchange effects. The TROSY-HSQC spectrum recorded at neutral pH (grey) (Figure S8) resembles the pH 4 spectrum, but lacks a number of resonances, mostly for the dynamically most disordered regions, including the linker between FP and NHR, as well as the IL loop. The RMSD between chemical shifts for residues that could be assigned at both pH 4 and pH 7 is 0.03 ppm for ^{1}H^N and 0.16 ppm for ^{15}N. The similarity between the resonance positions seen at acidic and neutral pH indicates that the protein structure is not significantly impacted by the difference in pH, as expected [7]. Due to the improved spectral characteristics at pH 4, all analysis is focused on the acidic pH condition. For spectra recorded in DDM (blue) the RMSD to chemical shifts in DPC spectra is 0.13 ppm for ^{1}H^N, 0.48 ppm for ^{15}N and 0.40 ppm for ^{13}C$^\alpha$, again indicating that the protein structure is quite similar under both detergent conditions. Because of reduced long-term stability of samples in DDM (< 4 weeks) compared to DPC (> 1 year), DPC was favored over DDM. Moreover, many of the amide resonances were broader and weaker in DDM, presumably due to a longer overall rotational correlation time associated with the larger micelle size.

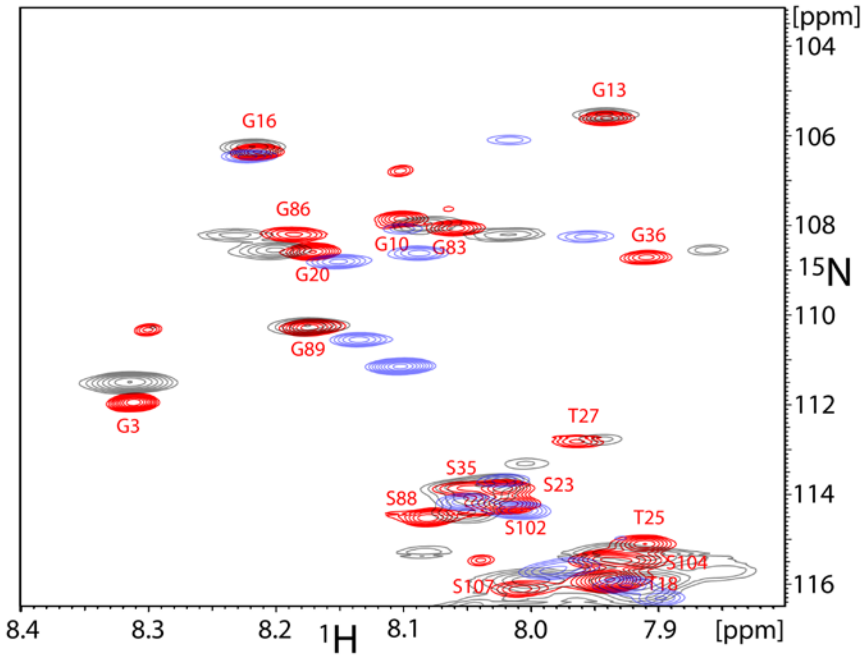

Figure S8. Overlay of 600 MHz ^{15}N-^{1}H TROSY-HSQC spectra of ^{2}H,^{15}N,^{13}C enriched gp41$^{1\text{-}194}$ solubilized in DPC, (pH 4 and 7.1) and DDM (pH 4), 40 °C. Shown is the most resolved region of the spectrum. Red contours correspond to DPC pH 4.0 (0.5 mM gp41$^{1\text{-}194}$, 330 mM DPC, 50 mM sodium acetate buffer; 25 mM KCl); transparent black contours correspond to DPC pH 7.1 (0.3 mM gp41$^{1\text{-}194}$, 200 mM DPC, 50 mM HEPES buffer, 25 mM KCl) and transparent blue contours correspond to DDM pH 4 (0.5 mM gp41$^{1\text{-}194}$, 150 mM DDM, 50 mM sodium acetate buffer, 100 mM NaCl).

2.2 Analysis of $^{13}C^{\alpha}$ secondary chemical shifts

As can be seen in Figure S9, the $^{13}C^{\alpha}$ secondary chemical shifts of FP show excellent agreement with those measured for the isolated FP in SDS micelles[13], indicating that the local secondary structure of FP is not impacted by the presence of the ectodomain or its incorporation in a homotrimeric assembly. While the $^{13}C^{\alpha}$ chemical shifts for the first 22 residues of gp41$^{1\text{-}194}$ are nearly identical to those seen for the isolated peptide in SDS micelles, from residue S23 onwards they increasingly diverge (Figure S9b). This result indicates that the succeeding NHR region in gp41$^{1\text{-}194}$, starting at Q29, influences the secondary structure adopted by the preceding linker region (A14 to V28) while the C-terminal region of the isolated FP lacks this stabilizing effect and is dynamically highly disordered, with essentially random coil characteristics.[13]

Using the program SPARTA+,[39] $^{13}C^{\alpha}$ chemical shifts can be predicted on the basis of X-ray crystallographic coordinates of a protein with an accuracy better than 1 ppm overall, and ca. 0.9 ppm for α-helical residues. $^{13}C^{\alpha}$ chemical shifts predicted for the ectodomain of gp41 on the basis of the X-ray structure (PDB entry 1AIK [22]) of a late fusion form, excluding the FP and TM regions, yields a pairwise $^{13}C^{\alpha}$ chemical shift root-mean-square difference relative to experimental values of only 0.62 ppm for the NHR region, indicating that the structure of this region in our gp41$^{1\text{-}194}$ construct must be very similar to that seen in the crystalline state. In this respect, it is important to note however, that $^{13}C^{\alpha}$ chemical shifts are not very sensitive to the presence or absence of nearby helices, and the close correspondence between observed and predicted shifts does not provide information on whether the ectodomain predominantly adopts the pre-fusion three-helical or the late fusion six-helical conformation.

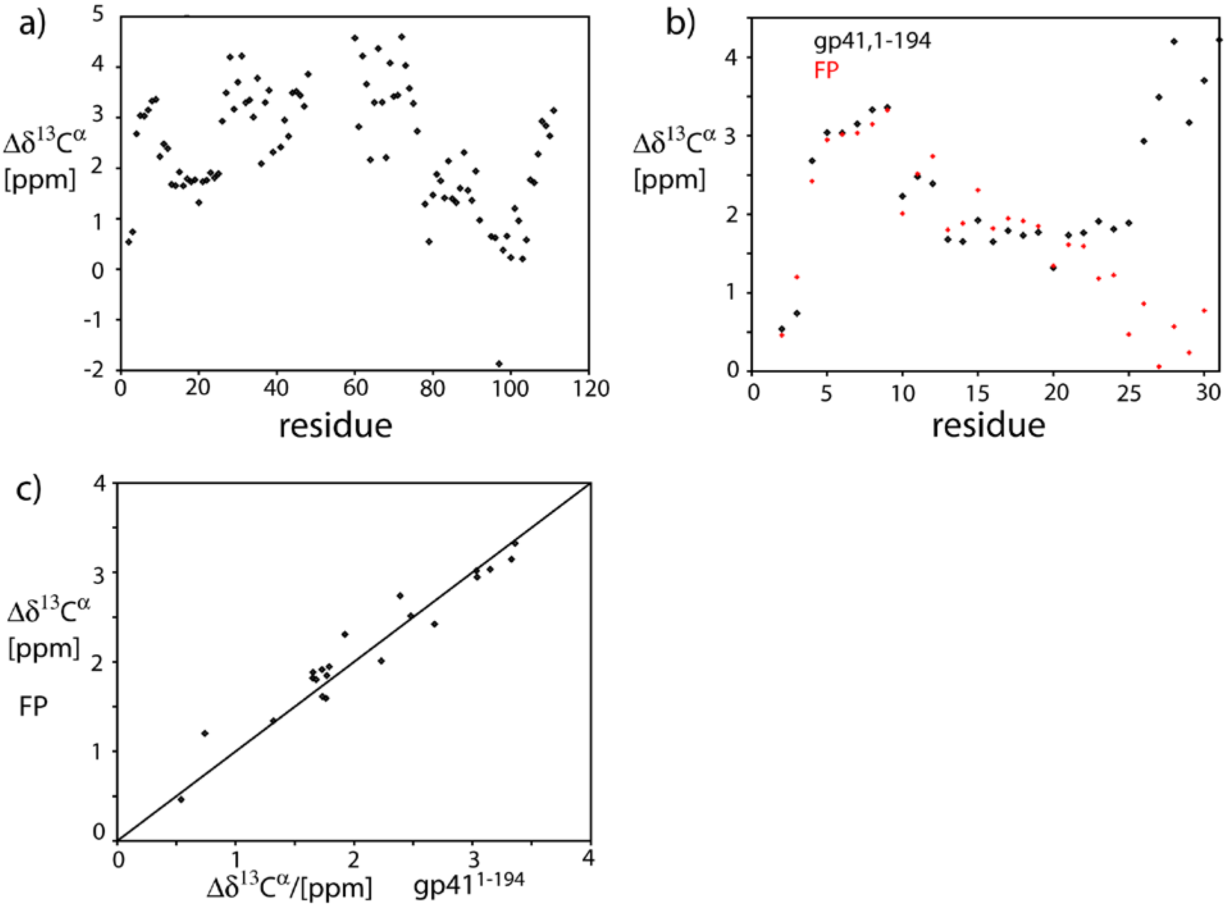

Figure S9. $^{13}C^{\alpha}$ secondary chemical shifts of gp41$^{1\text{-}194}$ in DPC micelles (^{2}H isotope shift correction was performed using the program TALOS+ [40]. a) Observed $^{13}C^{\alpha}$ secondary chemical shifts, $\Delta\delta^{13}C^{\alpha}$, showing a strong α-helical signature for the first 78 residues of gp41$^{1\text{-}194}$. Positive $\Delta\delta^{13}C^{\alpha} \approx 3 \pm 1.4$ ppm values are characteristic for stable α-helices. Residue V97 is followed by P98 and, as expected due to nearest neighbor effects[41], shows a negative secondary chemical shift. b) Comparison of $\Delta\delta^{13}C^{\alpha}$ values observed in the FP plus linker region of gp41$^{1\text{-}194}$ with values reported for the isolated FP, comprising residues 1-30 of gp41, preceded by an N-terminal Pro residue and followed by a C-terminal host tag[13]. c) Correlation graph of the $\Delta\delta^{13}C^{\alpha}$ values for the first 22 residues (V2-A22) of gp41, comparing values measured for gp41$^{1\text{-}194}$ and for isolated FP (residues S23-A30 of FP are highly disordered and therefore not included in the comparison). The Pearson's correlation coefficient, R, equals 0.97 and the pairwise root mean square difference (RMSD) equals 0.21 ppm.

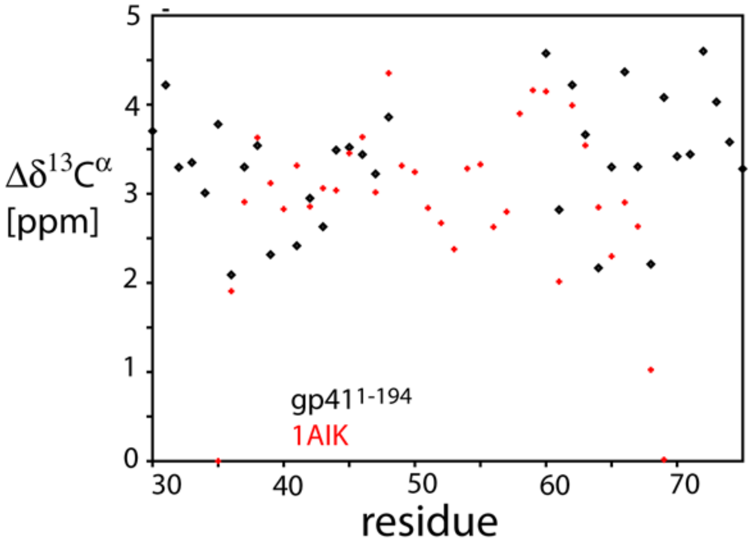

Figure S10. $^{13}C^{\alpha}$ secondary chemical shifts predicted for the ectodomain of the gp41 X-ray structure (red) (PDB entry 1AIK[22]) using the program SPARTA+[39] are compared to experimental values of gp41$^{1\text{-}194}$ in DPC micelles (black). ^{2}H isotope shift corrections were performed using values recently reported for fully disordered α-synuclein. [32]

2.3. Investigation of the presence of conformational exchange effects

The presence of conformational exchange contributions, R_{ex}, to the transverse relaxation rates of resonances visible in the gp41$^{1\text{-}194}$ spectrum is best evaluated by focusing on the transverse relaxation rate of the narrow, TROSY component of the ^{15}N magnetization, where conformational exchange has the largest fractional impact[42]. The exchange broadening effect is largest when measured in the Hahn-echo mode, and this type of measurement (using the pulse scheme of Figure S13) therefore was used to probe the presence of μs time scale dynamics in gp41$^{1\text{-}194}$. Measurements were carried out at two different magnetic field strengths, corresponding to 600 and 800 MHz ^{1}H frequency. Since R_{ex} scales with the square of the magnetic field, $R_{ex} \sim B_0^2$, a strong increase in the R_2 relaxation is expected for residues that are subject to conformational exchange effects. Such exchange effects seem to be largely absent for the visible part of the protein, with the exception of residues in the regions around A22, N42 and A96 (main text Figure 3e). As can be seen in Figure 3b of the main text, the effects of conformational exchange processes are found to be absent when evaluating R_2 rates extracted from a $T_{1\rho}$ measurement with a ^{15}N spin-lock RF field of 2 kHz (for details see Supporting Information section 3.2), indicating that the observed exchange process must be considerably slower than 500 μs/2π or ~80 μs.

2.4. PRE measurements

For measuring the effects of paramagnetic relaxation enhancement (PRE), a MTSL (*S*-(2,2,5,5-tetramethyl-2,5-dihydro-1H-pyrrol-3-yl)methyl) methanesulfonothioate, spin-label (Toronto Research Chemicals, Canada) was covalently attached to Cys-192 of the S192C mutant of gp41$^{1–194}$. MTSL from a 50 mM stock solution in 100% ethanol was added to 1 mg/ml gp41$^{1-194}$ to a 10-fold molar excess. The solution was incubated at room temperature for 48 hours. The labeled protein was concentrated to 1.5 ml using an Amicon-Ultra 15 ml, 30-kD concentrator (EMD Millipore) and then chromatographed on a S75 column as for the refolding.

Although PRE is often monitored simply in terms of the ratio of observed HSQC intensities in the absence and presence of the paramagnetic tag, such intensity ratios can be skewed by shortened proton T_1 times in the paramagnetic sample, in particular when the protein is perdeuterated, which will lead to a faster signal recovery and thus to an offset in the intensities of the paramagnetic sample versus the diamagnetic one. We therefore prefer to compare proton R_2 rates instead, as pointed out by Iwahara et al.[43] Proton R_2 rates were measured using a 2D TROSY-detected experiment as described by Anthis et al.[44] . Spectral settings were identical to those used for the ^{15}N R_1 and $R_{1\rho}$ measurement. Relaxation delays were sampled for 8 different durations (0, 20, 28, 4, 8, 12, 16, 24 ms). The total experimental time was 20 h. Spectra with identical settings were recorded for the paramagnetic MTSL-labeled and S192C gp41$^{1-194}$ samples as well as for the diamagnetic gp41$^{1-194}$ (wt) sample. To check the integrity of the spin-labeled sample, the paramagnetic MTSL label was quenched by a 10-fold excess of vitamin C that was incubated for 2 h at room temperature. Proton R_2 rates for the quenched samples were found to be in good agreement with the diamagnetic reference sample but had higher experimental uncertainty due to lower sample concentration.

Data collected for the S192C tagged protein (Fig. S11) show a small but consistent increase of ^{1}H R_2 rates by 8±2 s^{-1} for the N-terminal 25 residues, but no statistically significant change outside this region. The small but consistent increase in ^{1}H R_2 impacting nearly equally the first 25 residues suggests that transiently the fusion peptide and its linker to NHR come close to the micelle carrying the TM helix. However, considering how steeply PRE effects scale with distance and how uniform the effects are across the fusion peptide and its linker, these contacts never get close or specific, and must have a low population, suggesting that the late stage 6-helical bundle with proximity between TM and FP is at most lowly populated.

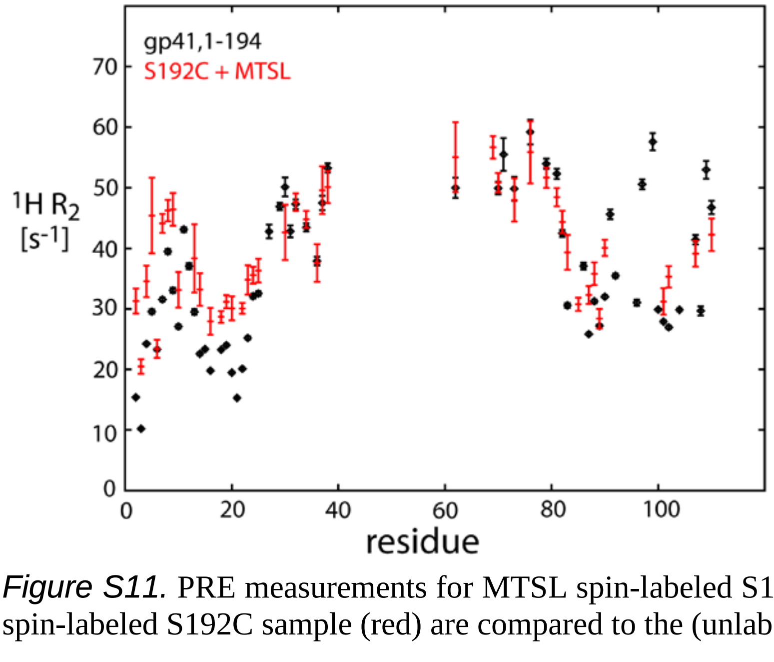

Figure S11. PRE measurements for MTSL spin-labeled S192C mutant of gp41$^{1-194}$. ^{1}H R_2 rates of the spin-labeled S192C sample (red) are compared to the (unlabeled) gp41$^{1-194}$ reference sample (black).

2.5. Measurement of $^{1}D_{NH}$ RDCs

A 0.25 mM uniformly ^{2}H,^{15}N- enriched gp41$^{1\text{-}194}$ sample (final concentration, solubilized in 150 mM DPC, 25 mM KCl, 50 mM sodium acetate buffer, pH 4) was soaked into a 4% w/v uncharged polyacrylamide gel (acrylamide:bisacrylamide ratio = 37:1) and radially compressed from 5.4 to 4.1 mm diameter (inner diameter of NMR sample tube) using a gel cylinder and funnel apparatus[45] (New Era Enterprises, Inc., USA). $^{1}D_{NH}$ RDCs were measured using the ARTSY method,[46] but RDCs appeared to be very weak (Figure S12), presumably due to the very extensive averaging resulting from internal dynamics. The poor spectral quality and consequently large RDC measurement errors did not allow a quantitative evaluation of the data.

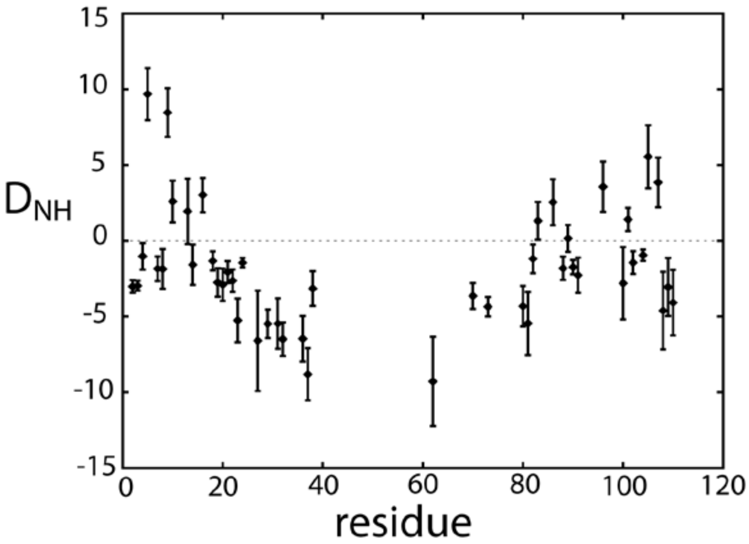

Figure S12. $^{1}D_{NH}$ RDCs were measured at 800 MHz ^{1}H frequency and 40 °C for a 0.25 mM uniformly ^{2}H,^{15}N- enriched gp41$^{1\text{-}194}$ sample (final concentration, solubilized in 150 mM DPC, 50 mM Na Ac, 25 mM KCl, pH 4) aligned in an uncharged 4% polyacrylamide gel. The signs of the RDCs follow the XPLOR-NIH convention, and do not account for the negative sign of the ^{15}N magnetogyric ratio.

3. Experimental details on NMR experiments

3.1. NMR backbone assignment experiments

Backbone assignment was performed using TROSY-based versions of the HNCO, HNCA, HNCB, HN(CO)CA and HN(CO)CB experiments[47, 48], carried out on a 600 MHz Bruker Avance II spectrometer, equipped with a TCI cryogenic probehead and a z-gradient accessory. All spectra were recorded at 40 °C. Backbone amide-selective three-dimensional H^N-H^N-NOESY-HMQC and $^{15}N^H$-$^{15}N^H$- HMQC-NOESY-HMQC experiments[49] were carried out on a 900 MHz Bruker Avance II spectrometer, equipped with a TXI cryogenic probehead and a z-gradient accessory. Triple resonance spectra were recorded using gradient echo/anti-echo encoding for TROSY selection[50] and mixed constant-time evolution[51] in the ^{15}N dimension to allow for long evolution times and high resolution. Spectral dimensions of the HNCO experiment were 1818 Hz (F_1) × 1471 Hz (F_2) × 8417 Hz (F_3), corresponding to 12 × 24.18 × 14.02 ppm, with sampling durations of 27.5 ms (t_1), 54.5 ms (t_2) and 100 ms (t_3). RF carriers were at 4.7 ppm for ^1H, 116 ppm for ^{15}N and at 176 ppm for ^{13}C. Eight scans per FID were recorded, with a recovery delay of 2 s between scans, resulting in a total experimental time of about 3.5 days. Spectral settings for the HNCA and HN(CO)CA experiments were identical to those for the HNCO experiment, except for the ^{13}C RF carrier set to 56 ppm and a full spectral width of 4504.51 Hz, corresponding to 29.86 ppm in the ^{13}C dimension, with a sampling duration of 11.1 ms (t_1) . Spectral settings for the HNCB and HN(CO)CB experiments differ only in the ^{13}C dimension, where a full spectral width of 10000 Hz was used, corresponding to 66.26 ppm, with a sampling duration of 10 ms (t_1) and the ^{13}C RF carrier at 43 ppm. The transfer time from $^{13}C^\alpha$ to $^{13}C^\beta$ was set to 2×7.2 ms, such that the $^{13}C^\alpha$ magnetization is fully transferred to $^{13}C^\beta$. Four scans per FID were recorded, resulting in a total experimental time of 3d 8h. Three-dimensional H^NH^N-NOESY-HMQC and $^{15}N^H$-$^{15}N^H$-HMQC-NOESY-HMQC experiments were recorded at 900 MHz with a 200 ms NOE-mixing time. Backbone amide selective EBURP and time-reversed EBURP ^1H 90^0 pulses and IBURP-2 ^1H 180^0 pulses[52] were used for limiting the excitation to the resonances of interest, and to obtain improved water suppression. Spectral dimensions of the H^NH^N-NOESY-HMQC experiment were 1805 Hz (F_3) × 2000 Hz (F_2) × 9014 Hz (F_3), corresponding to 2.00 × 21.9 × 10 ppm, with sampling durations of 22.2 ms (t_1), 26 ms (t_2) and 100 ms (t_3). RF carriers were at 8 ppm for ^1H, 116 ppm for ^{15}N and at 176 ppm for ^{13}C. Four scans per FID were recorded, with a recovery delay of 2s between scans, resulting in a total experimental time of about 1.5 days. Spectral settings for the $^{15}N^H$-$^{15}N^H$ -HMQC-NOESY-HMQC were identical to the H^NH^N-NOESY-HMQC, except for the F_1 dimension which was ^{15}N instead of ^1H, resulting in spectral dimensions of 2000 Hz (F_1) × 2000 Hz (F_2) × 9014 Hz (F_3), corresponding to 21.9 × 21.9 × 10 ppm, with sampling durations of 20 ms (t_1), 26 ms (t_2) and 100 ms (t_3).

3.2. ^{15}N Relaxation and ^{15}N-{^1H} NOE experiments

Spectra were recorded at 40 °C on a 600 MHz Avance II Bruker and on a 800 MHz Avance III Bruker spectrometer, equipped respectively with a TCI and TXI cryogenic probehead, each with a z-gradient accessory. ^{15}N relaxation rates were recorded by TROSY-based methods as described recently.[19] Spectral dimensions were 1805 Hz (F_1) × 8417 Hz (F_2) for the measurement at 600 MHz, corresponding to 30.1 × 14 ppm, with sampling durations of 66 ms (t_1) and 122 ms (t_2). For the measurement at 800 MHz, spectral dimensions were 2500 Hz (F_1) × 11161 Hz (F_2), corresponding to 14 ppm × 31.25 ppm, with sampling durations of 48 ms (t_1) and 92 ms (t_2). Relaxation delays were sampled for 8 different delay durations (^{15}N R_1 delays: 0, 240, 400, 640, 800, 1040, 1200, 1600 ms at 600 MHz and 0, 800, 80, 1600, 400, 1200, 1000, 1400 ms at 800 MHz; ^{15}N $R_{1\rho}$ delays 10, 1, 20, 40, 30, 50, 15, 35 ms at 600 MHz and 10, 40, 1, 30, 20, 35, 25, 15 ms at 800 MHz). The strength of the RF spin-lock field during the $R_{1\rho}$ measurement was ν_{RF} = 2 kHz. RF carriers were at 4.6 ppm for ^1H, 118 ppm for ^{15}N and at 176 ppm for ^{13}C. Sixteen scans per FID were recorded, with a recovery delay of 2 s between scans, resulting in total experimental times of about 32 h for the R_1 measurements and 20 h for the $R_{1\rho}$ experiments.

The ^{15}N-{^{1}H} NOE and reference spectra were recorded in an inter-leaved manner with a 5 s ^{1}H saturation time for the NOE experiment and the equivalent recovery time for the reference experiment, each preceded by an additional 1 s recovery time. Spectral settings were identical to those for the R_1 and $R_{1\rho}$ measurement; but 48 scans were recorded per FID, resulting in total experimental times of ca. 48 h. Spectra were processed and analyzed with the NMRPipe program, [31] as described previously. [19]

3.3. ^{15}N TROSY-T$_2$ experiment

Conformational exchange contributions, $R_{ex,}$ to transverse ^{15}N relaxation rates, R_2, were studied by measuring ^{15}N R_2 relaxation of the slowly relaxing doublet component in a TROSY-HSQC spectrum using the pulse scheme of Figure S13. Due to the partial cancellation between ^{15}N-^{1}H dipolar and ^{15}N CSA R_2 mechanisms for the TROSY component of the ^{15}N-{^{1}H} doublet, the fractional increase of its R_2 caused by R_{ex} is higher than for a regular R_2 measurement, making it advantageous to detect such effects using the TROSY component of ^{15}N magnetization.[42] By measuring the R_{ex} contribution in a Hahn-echo mode, exchange effects over the widest possible range of time scales is detected. This contrasts with $T_{1\rho}$ or Carr-Purcel-Meiboom-Gill (CPMG) type experiments which eliminate exchange effects on time scales slower than the effective RF frequency of the spin-lock field or CPMG block. Since R_{ex} scales with the square of the magnetic field, $R_{ex} \sim B_0^2$, comparison of such “TROSY-R_2” rates, measured at two different fields provides a convenient and unambiguous way for identifying residues that are subject to conformational exchange.

“TROSY-R_2” rates were measured at 600 MHz and 800 MHz, with the relaxation delay sampled for two delay durations (Δ=0 and Δ=25 ms, at both 600 and 800 MHz). Spectral settings were identical to those for the ^{15}N R_1 and R_2 measurements, reported above, with a total experimental time of ~19 h.

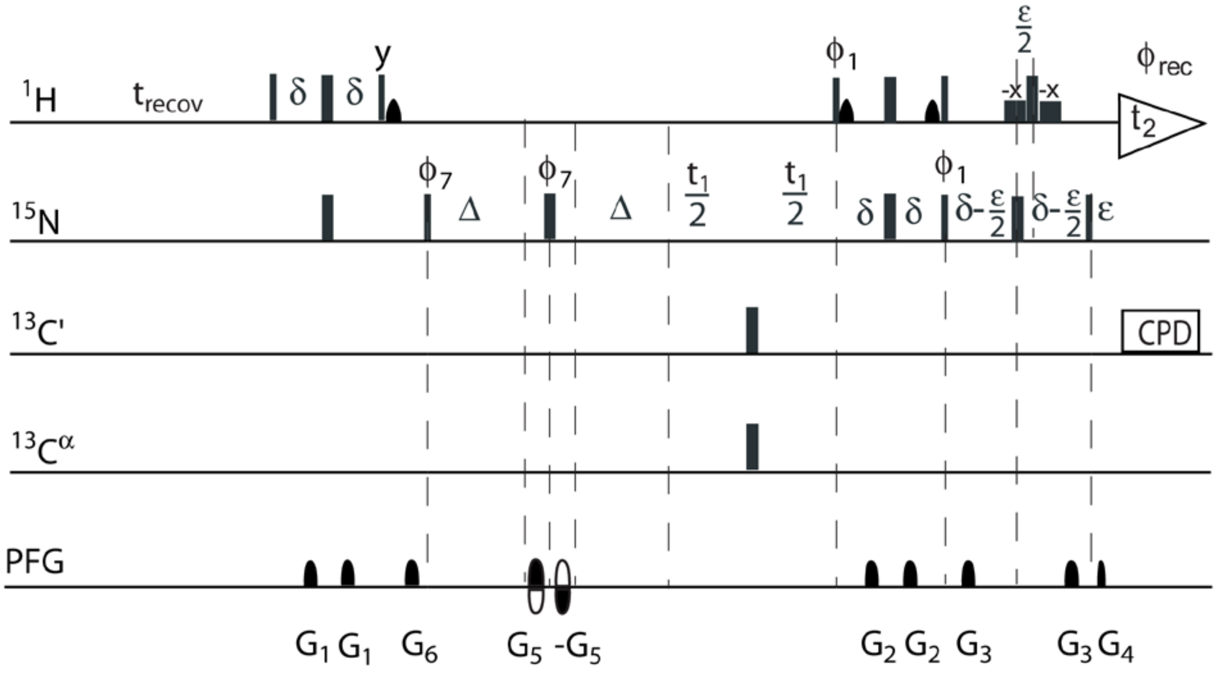

Figure S13. Pulse scheme used for measurement of the relaxation rates of the slowly relaxing ^{15}N-{^{1}H} doublet component in U-^{2}H/^{13}C/^{15}N, amide-protonated gp41$^{1-194}$ using a Hahn echo (Δ – 180^0(N) – Δ) element during the echo/anti-echo gradient encoding step. The rectangular ^{1}H pulses marked –x are low power 90° pulses (1.2 ms at 600 MHz); shaped low power ^{1}H pulses (1.9 ms) correspond to the center lobe of a (sin*x*)/*x* function, all serving to return the water magnetization to z prior to detection.[53] For application to samples that also are enriched in ^{13}C: durations of ^{13}C pulses (all 180°)

are equal to $\frac{\sqrt{3}}{2\Omega}$ (47.4 μs at 600 MHz), where Ω is the frequency difference between $^{13}C^{\alpha}$ and $^{13}C'$. Delay durations are δ = 2.65 ms and ε corresponds to the duration of the decoding gradient G_4 (60.8 μs; the slight offset ($\varepsilon/2$) relative to the ^{15}N 180° pulse enables insertion of the decoding gradient G_4, without introducing a linear phase error in the ^{1}H dimension. Gradients: G_1 (200 μs; 1.4 G/cm), G_2 (300 μs; 7 G/cm), G_3 (1 ms; 35 G/cm), G_4 (60.8 μs; 23 G/cm), G_5 (300 μs; -23 G/cm) and G_6 (1 ms; 21 G/cm) are sine-bell shaped. Phase cycling: φ_7=y,x,-y,-x; φ_1 = y; φ_{rec}=y,-x,-y,x. Quadrature detection is implemented using the Rance-Kay echo/anti-echo scheme[54] with the polarity of gradients G_5 and $-G_5$ inverted, and phase φ_7=y,-x,-y,x and φ_1 = -y for the second FID generated for each quadrature pair. The relaxation decay of the slowly relaxing ^{15}N-{^{1}H} doublet component is sampled at different delay durations Δ in an inter-leaved manner.

3.4. Experiment for the measurement of transverse ^{15}N CSA-dipolar cross-correlated relaxation ^{15}N η_{xy}

The transverse ^{15}N CSA-dipolar cross-correlated relaxation rate, η_{xy}, was determined by measuring the difference in relaxation rate between the slowly and fast relaxing NH doublet component according to

$$R_{2,\beta} = R_{2,0} - \eta_{xy} + R_H + R_{ex} \quad (1a)$$
$$R_{2,\alpha} = R_{2,0} + \eta_{xy} + R_H + R_{ex} \quad (1b)$$
$$2\eta_{xy} = R_{2,\alpha} - R_{2,\beta} \quad (1c)$$

where $R_{2,\alpha/\beta}$ is the relaxation rate of the fast/slowly relaxing doublet component, $R_{2,0}$ is the R_2 auto-relaxation, η_{xy} is ^{15}N CSA-dipolar cross-correlated relaxation, R_H is the dipolar relaxation with remote protons and R_{ex} is the conformational exchange contribution.

As can be seen from equation 1, measurement of η_{xy} data is not affected by conformational exchange (R_{ex}) contributions and thus provides useful additional information to estimate the overall tumbling correlation time τ_c.[30] The two-dimensional extension of the original TRACT experiment[30] detects the slowly and fast relaxing doublet components in the indirect dimension (with detection taking place on the slowly relaxing line in the detected ^{1}H dimension in both cases) in an interleaved manner. However, that experiment suffers from line broadening and reduced S/N for the fast relaxing doublet line in the indirect dimension. Here, we use a slightly different scheme, shown in Figure S14. In this scheme, the relaxation rate of the slowly relaxing ^{15}N doublet line is measured in the same manner as for the TROSY-T_2 experiment. To measure the relaxation rate of the fast relaxing doublet line, prior to the echo-/anti-echo encoding step, the fast and slowly relaxing component are interchanged by a 180° ^{1}H pulse and flipped back again by a second 180° ^{1}H pulse just prior to t_1 evolution, such that the magnetization is subject to fast relaxation (2) during the relaxation period but to slow relaxation during the t_1 evolution. Thus, also for the spectrum that measures the decay of the fast relaxing line, the slowly relaxing "TROSY" line is detected both for the indirect and direct dimension, thereby optimizing resolution and sensitivity.

The relaxation decay was sampled at 6 different points (1, 26, 11, 21, 16 and 6 ms, both at 600 and 800 MHz). Sampling points were optimized for measurement of the fast relaxing doublet line, and $R_{2,\beta}$ and $R_{2,\alpha}$ relaxation were measured in an interleaved manner. The transverse cross-correlated relaxation rate has been extracted from the difference of the $R_{2,\beta}$ and $R_{2,\alpha}$ rate (equation 1c).

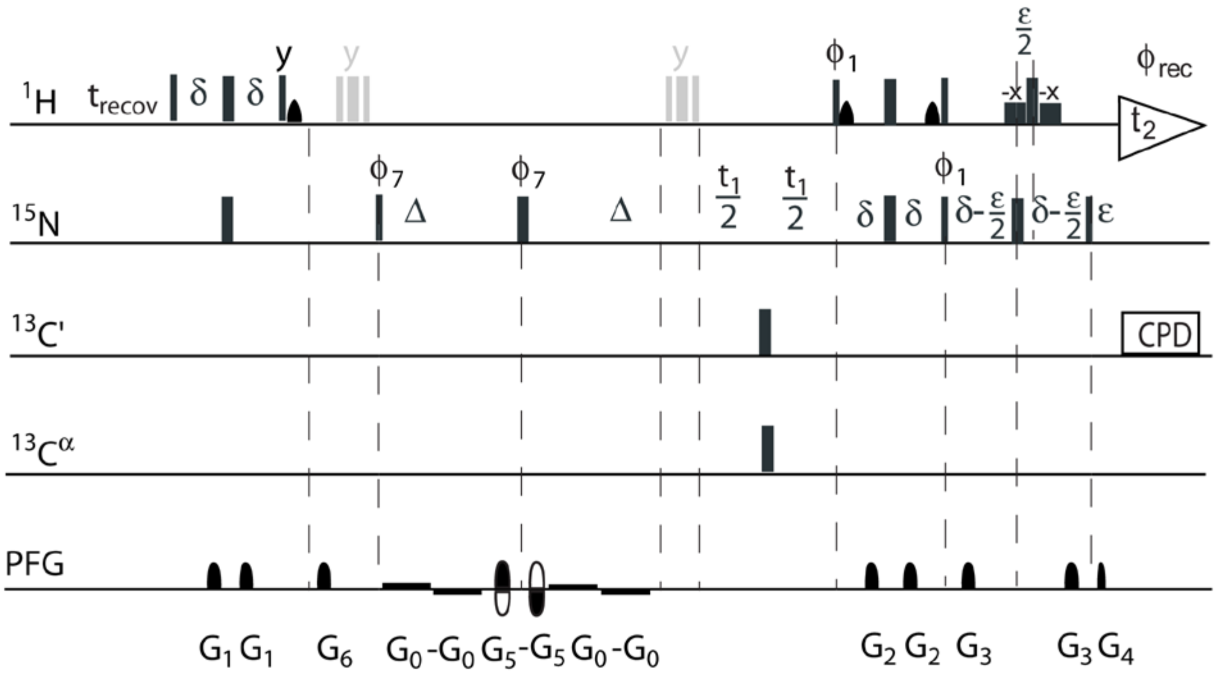

Figure S14. Pulse scheme for measurement of transverse ^{15}N CSA-dipolar cross-correlated relaxation rates, η_{xy}, in perdeuterated, amide-protonated proteins. The relaxation decay rates of the slowly and fast relaxing NH doublet components are measured during a Hahn echo element with variable delay Δ (Δ - 180°(^{15}N) – Δ) in an inter-leaved manner. For the slowly relaxing doublet component, the sequence is identical to the "TROSY-T2" experiment of Figure S13. For the fast relaxing doublet component, prior to the ^{15}N coherence encoding and Hahn echo, a composite 90_x-210_y-90_x ^{1}H pulse (grey) is applied to interchange the fast and slowly relaxing ^{15}N-{^{1}H} doublet components. After the Hahn echo, a second composite 90_x-210_y-90_x proton pulse is applied prior to t_1 evolution, to switch back the fast and slowly relaxing doublet components, such that the TROSY component is active during t_1 evolution and detection, and the fast relaxing anti-TROSY component is active only during the Hahn echo relaxation delay. All other parameters are the same as for Figure S13.

4. Extended model-free analysis

NMR relaxation data were analyzed using the model-free analysis of Lipari and Szabo.[24, 26] First, as input for the model-free analysis, clusters of residues with similar dynamic properties (I4-L12, Q29-R46, I62-L76, T18-M24, G86-N105) were identified. For each experimental rate (R_1, R_2, η_{xy} or I/I_0) and each cluster *c*, an error-weighted average rate $<r>_{c,err}$ and the error-weighted standard deviation of the rates in the cluster $<\sigma>_{c,err}$ were calculated. This was done in the following way: For each experimental individual rate *r* in the cluster, a Gaussian normal distribution $N(r, \sigma(r))$ was assumed with standard deviation $\sigma(r)$ equal to the experimental uncertainty Δr of the rate *r*, $\sigma(r)= \Delta r$. Now (to simulate the impact of uncertainty Δr of the individual rate *r* of residue X in the cluster *c* on the average value $<r>_c$ and standard deviation $<\sigma>_c$) a new cluster was generated: Instead of taking the experimental rate *r* for residue X, a random sample from the Gaussian distribution $N(r, \sigma(r))$ was taken. This was repeated N=1000 times. In this manner, a 1000-fold larger cluster c_{1000} was generated which reflects the experimental uncertainty. The error-weighted average rate $<r>_{c,err}$ then was determined by calculating the average rate of the cluster c_{1000}, $<r>_{c,err} = <r>_{c, 1000}$ and the error-weighted standard deviation was determined by calculating the standard deviation of the rates in the cluster c_{1000} , $<\sigma>_{c,err} = <\sigma>_{c,1000}$. As expected the error weighted average rate $<r>_{c,err}$ agrees very closely with the average value of the experimental rates $<r>$. Error-weighted average values and standard deviations of the different clusters are presented in Table S2a.

To describe the dynamics of the FP relative to the NHR, relaxation data for the different clusters shown in Table S2a were analyzed using the model-free approach,[26] implemented with an in-house written MATLAB script. A libration-corrected NH bond length of r_{NH} = 1.04 Å [55] was used, thereby removing the effect of normal mode librations and yielding an upper limit for the fast motion internal order parameter of S_f^2 =1. A ^{15}N CSA value of $\Delta\sigma$ = -173 ppm, applicable for α-helical residues[56] was used. Parameters were fitted to R_1, R_2 and ^{15}N-{^{1}H} NOE data, as well as η_{xy} data. All data were fitted to experimental data recorded at two fields, 600 and 800 MHz, using a grid search χ^2 minimization procedure. From the η_{xy} data, a lower limit for the rotational correlation time was determined to be $\tau_c \geq$ 28ns, using a rigid rotor assumption for the most rigid residue cluster (I62-L76). In a first attempt, we tried to fit the data by the standard model-free approach, using as variables the rotational correlation time τ_c, the fast internal correlation time τ_f, and the order parameter S_f^2. The resulting fit leads to local correlation times τ_c between 10 ns and 25 ns, far below the limit obtained from the η_{xy} data, and unusual internal correlations times τ_f of up to 240 ps (which was the boundary of the grid), and even with these parameters the R_1 or R_2 values could not be properly fit. Indeed, as pointed out previously [25, 57] the underestimated rotational correlation time τ_c as well as overestimated internal correlation time τ_f are a fitting artifact resulting from the failure of the simple model-free approach to capture slow nanosecond dynamics. Anisotropy of the diffusion tensor as the sole explanation[58] can be excluded, since τ_c was included in the fit and even when *local* correlation times τ_c were used as free parameters none of the data points could be fitted using the simple model-free approach.

Next we analyzed the data using the extended model-free approach[24] with a slow internal correlation time, τ_s, and a slow internal order parameter, S_s^2, as additional parameters to characterize low nanosecond motions that are slower than the overall tumbling correlation time τ_c. All five clusters were simultaneously fitted to a global correlation time τ_c and each cluster individually with (S_f^2, S_s^2, τ_s) as free parameters. The fast internal correlation time τ_f was fixed to τ_f =50 ps to reduce the parameter space, leaving 16 fitting parameters for 40 data points per cluster. The grid search was performed first with a wider grid to ensure full sampling and correct estimation of the boundaries of the parameter space at reasonable computation times and this initial search was followed by a second finer search using a narrower grid. The parameter space of the final narrow grid was (τ_c = 30,31, …. 65 ns; S_f^2 =1.00, 0.99, …, 0.75; τ_f = 50 ps; S_s^2 =1.00, 0.99, …, 0.55; τ_s = 2.0, 2.1, …, 6.0 ns). For fitting to the experimental data, a global minimum of the χ^2 minimization was reached for τ_c= 44±3 ns. Error estimates for all fitting parameters were calculated using the Monte-Carlo method with N=500, assuming a Gaussian normal distribution with standard deviation equal to the experimental error. Best-fit parameters, characterizing the internal dynamics of the five clusters are shown in Table 1 (main manuscript) and duplicated in Table S2b for easy comparison. Back-calculated data agree with the experimental input data to well within their standard deviations (compare Table S2c and S2a).

Table S2a. Average experimental data and error-weighted standard deviation for clusters of residues with similar dynamic properties in gp41$^{1\text{-}194}$.

	R_1 [s^{-1}] 600 MHz	R_1 [s^{1}] 800MHz	R_2 [s^{-1}] 600 MHz	R_2 [s^{-1}] 800MHz	I/I_0 600MHz	I/I_0 800MHz	η_{xy} 600MHz	ηxy 800MHz
I4-L12	1.14 ±0.03	0.91 ±0.03	23.15 ±1.7	28.4 ±2.0	0.57 ±0.05	0.65 ±0.05	16.0 ±1.6	20.7 ±1.6
Q29-R46	0.98 ±0.04	0.77 ±0.03	33.9 ±1.7	40.6 ±1.9	0.58 ±0.05	0.67 ±0.04	24.0 ±1.6	31.9 ±2.5
I62-L76	0.86 ±0.05	0.66 ±0.04	41.9 ±3.3	52.8 ±2.3	0.62 ±0.09	0.64 ±0.06	28.9 ±3.6	35.2 ±2.7
T18-M24	1.23 ±0.04	1.06 ±0.04	15.2 ±2.0	19.1 ±2.2	0.32 ±0.02	0.46 ±0.02	10.0 ±1.5	13.6 ±1.9
G86-N105	1.14 ±0.04	0.98 ±0.06	20.5 ±2.8	25.8 ±3.0	0.35 ±0.07	0.47 ±0.05	13.4 ±2.4	17.8 ±3.0

Table S2b. Results of the extended model-free analysis (copied from Table 1 in the main manuscript).

Cluster	τ_c [ns]	$\boldsymbol{S}^2_f$	τ_f [ps]	τ_s [ns]	$\boldsymbol{S}^2_s$
I4-L12	44±3	0.77±0.02	50	5.4±0.7	0.42±0.04
Q29-R46	44±3	0.85±0.02	50	4.0±0.9	0.64±0.05
I62-L76	44±3	0.90±0.04	50	3.1±0.9	0.76±0.03
T18-M24	44±3	0.62±0.02	50	2.3±0.2	0.37±0.02
G86-N105	44±3	0.67±0.03	50	2.5±0.7	0.48±0.04

Table S2c. Back-calculated relaxation data using the model-free parameters shown in Table S1b.

	R_1 [s^{-1}] 600 MHz	R_1 [s^{-1}] 800 MHz	R_2 [s^{-1}] 600 MHz	R_2 [s^{-1}] 800 MHz	I/I_0 600 MHz	I/I_0 800 MHz	η_{xy} 800 MHz	η_{xy} 800 MHz
I4-A4	1.15 ±0.02	0.89 ±0.02	22.4 ±0.85	27.2 ±1.05	0.59 ±0.03	0.60 ±0.03	16.9 ±0.65	22.4 ±0.87
Q29-R46	0.97 ±03	0.77 ±0.03	33.3 ±0.99	40.8 ±1.22	0.62 ±0.04	0.64 ±0.03	25.3 ±0.75	33.5 ±1.01
I62-L76	0.82 ±003	0.67 ±0.03	40.8 ±1.42	50.0 ±1.75	0.63 ±0.04	0.68 ±0.05	31.0 ±1.08	41.1 ±1.44
T18-M24	1.21 ±0.03	1.11 ±0.03	15.2 ±1.00	18.5 ±1.24	0.34 ±0.02	0.43 ±0.02	11.5 ±0.76	15.2 ±1.02
G86-N105	1.13 ±0.03	1.00 ±0.05	20.2 ±1.48	24.7 ±1.83	0.39 ±0.05	0.46 ±0.03	15.3 ±1.12	20.3 ±1.50

5. NMR backbone assignment data

97 out of about 110 spin systems visible in the HNCO spectrum could be assigned. In addition to these 110 spin systems, a minor population (< 20 %) of the fusion peptide could be identified in which oxidation of the M19 and M24 results in a second set of peaks for the fusion peptide resonances for residues G10-A22. The cause of oxidation could be traced back to interaction with peroxidized lipids present during the expression protocol. Their presence in several of the protein preparations was decreased (to <12%) using butylated hydroxytoluene (BHT, Sigma-Aldrich, USA). Resonances for both forms of the protein can be clearly distinguished. Results below pertain only to the major component of the FP, in the absence of oxidation of M19 and M24.

Table S3. Chemical shift assignment for the studied gp41$^{1-194}$ construct in DPC micelles.

AA	$\delta(^{1}\mathrm{H})$[a]	$\delta(^{15}\mathrm{N})$	$\delta(^{13}\mathrm{C'ii\text{-}1}))$	$\delta(\mathrm{C}^{\alpha})$	$\delta(\mathrm{C}^{\beta})$
	[ppm]	[ppm]	[ppm]	[ppm]	[ppm]
V2	8.59	119.9	173.8	62.0	32.3
G3	8.32	111.9	175.7	45.1	-
I4	8.59	121.8	174.8	63.2	37.1
G5	8.94	110.4	177.3	47.4	-
A6	7.98	123.5	175.2	54.4	17.7
L7	7.87	120.3	181.0	57.4	41.0
F8	8.23	118.9	178.9	60.8	38.6
L9	8.36	118.6	177.3	57.6	40.4
G10	8.11	107.9	180.0	46.5	-
F11	7.97	122.7	176.3	59.9	38.4
L12	7.91	118.4	176.7	56.6	40.9
G13	7.95	105.6	178.6	46.0	-
A14	7.80	124.3	175.3	53.0	18.2
A15	8.11	121.9	178.7	53.3	17.9
G16	8.22	106.3	178.7	46.0	-
S17	7.94	116.0	175.7	59.4	63.6
T18	7.94	115.9	175.0	63.2	68.9
M19	8.09	120.8	175.3	56.4	32.1
G20	8.18	108.6	177.0	45.6	-
A21	8.01	124.1	174.7	53.1	18.3
A22	8.14	121.7	178.5	53.1	18.2
S23	8.03	113.8	178.3	59.6	63.4
M24	8.03	122.1	175.3	56.4	31.9
T25	7.92	115.2	176.8	63.4	69.0
L26	8.20	122.7	175.5	57.2	40.8
T27	7.97	112.8	178.2	65.0	68.6
V28	7.73	121.9	176.2	65.7	31.1
Q29	8.08	119.6	178.5	58.3	27.7
A30	8.42	122.3	178.7	55.1	17.8
R31	8.12	117.1	178.9	59.6	29.1
Q32	7.97	119.3	178.9	58.4	27.6
L33	7.98	121.7	176.6	57.6	41.2
L34	8.09	118.2	178.9	57.2	40.9
S35	8.03	113.8	178.3	61.4	63.4
G36	7.91	108.7	176.7	46.4	-

I37	7.77	121.2	175.8	63.8	37.4
V38	7.82	117.9	177.4	65.0	31.8
Q39	7.86	118.7	177.8	57.4	28.2
Q41	7.96	119.6	176.9	57.5	27.5
N42	8.21	118.6	176.3	55.5	38.3
N43	8.24	119.0	176.6	55.1	38.6
L44	8.13	122.6	177.3	57.7	41.0
L45	8.04	119.0	178.1	57.7	nd
R46	8.14	118.6	178.5	58.9	nd
A47	7.69	122.1	178.9	54.6	17.6
I48	8.00	118.0	180.1	64.4	37.3
W60	8.00	120.6	179.3	61.4	27.4
G61	8.85	107.7	178.6	47.1	-
I62	8.46	122.2	175.1	64.7	36.5
K63	8.02	120.3	177.9	59.3	30.6
Q64	7.89	119.2	180.2	57.3	27.5
L65	7.97	120.5	176.4	57.5	40.9
Q66	8.47	119.1	178.5	59.5	27.8
A67	7.71	119.9	177.5	54.7	17.4
R68	7.70	118.3	180.8	57.6	29.0
I69	8.06	118.9	179.1	64.6	36.5
L70	8.09	120.4	177.8	57.6	40.5
A71	7.58	121.5	179.5	54.8	17.5
V72	7.92	119.3	180.7	66.1	30.7
E73	8.38	119.6	177.6	59.7	27.3
R74	8.05	118.7	178.0	59.0	29.0
Y75	7.78	120.3	174.6	60.8	37.8
L76	8.18	117.9	177.7	56.9	40.9
D78	7.90	119.4	nd	54.7	41.1
Q79	7.84	118.6	176.7	55.7	27.7
Q80	8.03	118.3	176.1	56.6	27.4
L81	8.04	120.4	176.8	56.1	41.5
L82	7.94	118.2	177.4	56.0	41.1
G83	8.06	108.1	178.4	45.7	-
I 84	7.72	120.0	175.4	62.7	37.5
W85	7.98	121.8	179.1	58.2	29.4
G86	8.19	108.2	177.4	45.6	-
A87	7.94	123.7	174.8	53.0	18.4
S88	8.08	114.5	178.6	60.0	63.5
G89	8.18	110.3	175.5	45.9	-
K90	7.80	120.4	174.6	57.0	31.8
L91	7.94	121.3	177.3	56.2	41.3
I92	7.78	118.8	177.7	61.5	37.5
T95	7.75	115.5	174.8	62.1	69.3
A96	8.03	125.8	173.9	52.0	18.7
V97	7.72	118.9	176.9	59.6	31.5
P98				62.8	30.3
W99	7.65	119.8	176.2	57.4	28.9
N100	7.69	119.0	175.6	52.7	38.2
A101	7.89	124.3	174.8	52.6	18.4
S102	8.02	114.2	177.5	58.6	63.4

W103	7.96	122.7	176.3	57.0	28.9
S104	7.93	115.5	177.5	58.2	63.6
N105	8.31	121.0	174.5	54.3	38.2
K106	8.12	121.5	175.9	57.3	31.8
S107	8.01	116.1	177.6	59.9	63.3
L108	8.23	122.6	176.0	57.2	40.8
E109	8.08	117.5	178.3	58.6	27.7
Q110	7.75	117.5	177.9	57.8	27.9
I111	7.68	118.7	178.1	63.7	38.2

[a] Backbone assignment for uniformly $^{2}H/^{15}N/^{13}C$-enriched homotrimeric gp41$^{1-194}$ at 40 °C (50 mM sodium acetate, pH 4.0, 25 mM KCl and 330 mM (≈ 115 mg/ml) DPC. The raw experimental data are presented (before isotope shift correction).

6. ^{15}N relaxation data

Table S4a. ^{15}N R_1 and ^{15}N R_2 relaxation data for gp41$^{1\text{-}194}$, measured at 600 and 800 MHz.

#	R_2 [s^{-1}]^a	ΔR_2 [s^{-1}]	R_1 [s^{-1}]	ΔR_1 [s^{-1}]	R_2 [s^{-1}]	ΔR_2 [s^{-1}]	R_1 [s^{-1}]	ΔR_1 [s^{-1}]
	600MHz		600MHz		800 MHz		800 MHz	
V2	4.7	0.1	1.10	0.01	5.6	0.0	1.04	0.01
G3	6.1	0.1	1.37	0.01	7.7	0.1	1.26	0.01
I4	19.4	0.2	1.15	0.01	24.1	0.2	0.93	0.01
G5	21.6	0.3	1.16	0.02	26.5	0.3	0.95	0.02
L7	24.0	0.2	1.15	0.01	28.6	0.2	0.90	0.01
F8	24.8	0.3	1.11	0.01	30.3	0.3	0.88	0.01
L9	24.5	0.3	1.16	0.02	29.4	0.3	0.90	0.01
G10	23.1	0.3	1.13	0.02	27.7	0.3	0.89	0.01
F11	23.5	0.2	1.11	0.01	30.1	0.2	0.91	0.01
L12	24.4	0.3	1.11	0.02	30.0	0.3	0.89	0.01
G13	21.0	0.3	1.15	0.02	24.9	0.4	0.92	0.02
A14	19.0	0.2	1.19	0.01	24.1	0.2	1.00	0.01
A15	17.5	0.1	1.15	0.01	21.7	0.2	0.96	0.01
G16	14.7	0.1	1.19	0.01	17.9	0.2	1.00	0.01
T18	13.4	0.1	1.24	0.01	17.2	0.1	1.08	0.01
M19	15.9	0.1	1.25	0.01	19.6	0.1	1.07	0.01
G20	12.6	0.1	1.27	0.01	16.3	0.1	1.11	0.01
A21	13.0	0.1	1.27	0.01	16.9	0.1	1.10	0.01
A22	16.4	0.1	1.19	0.01	20.7	0.1	1.01	0.01
S23	16.6	0.1	1.15	0.01	19.9	0.1	0.99	0.01
M24	18.4	0.2	1.24	0.02	22.9	0.2	1.04	0.01
T25	20.8	0.2	1.16	0.01	24.8	0.2	0.95	0.01
T27	28.0	0.7	1.03	0.03	35.4	0.7	0.79	0.02
Q29	35.1	0.6	1.00	0.01	40.8	0.5	0.77	0.01
A30	35.6	1.4	0.99	0.03	39.8	1.3	0.78	0.03
R31	31.8	0.8	0.98	0.02	39.4	0.8	0.74	0.02
Q32	33.9	0.7	1.00	0.02	42.1	0.6	0.78	0.01
L34	34.9	0.7	0.99	0.02	41.9	0.6	0.74	0.01
G36	31.8	0.6	0.92	0.02	39.6	0.6	0.79	0.01
I37	34.2	1.1	0.97	0.03	41.6	1.0	0.77	0.02
V38	34.0	0.6	0.92	0.01	42.9	0.7	0.77	0.02
Q41	33.1	1.0	1.02	0.03	37.6	1.2	0.80	0.03
L44	32.5	1.1	1.01	0.03	38.3	1.1	0.79	0.03
R46	36.2	0.9	0.97	0.02	42.6	0.9	0.72	0.02
A47	40.5	1.8	0.95	0.04	50.1	1.7	0.76	0.03
I62	41.9	1.8	0.81	0.03	52.3	1.5	0.63	0.02
L65	42.8	0.9	0.85	0.01	51.4	0.8	0.67	0.01
R68	nd	nd	nd	nd	55.4	2.7	0.64	0.03
E73	37.5	1.8	0.92	0.04	52.0	1.6	0.70	0.02

L76	45.5	2.1	0.87	0.03	55.0	2.0	0.69	0.03
Q79	37.3	0.8	0.95	0.02	48.4	0.8	0.74	0.01
Q80	37.8	0.9	0.89	0.02	46.9	0.9	0.75	0.02
L81	33.3	0.6	0.93	0.02	41.1	0.7	0.75	0.01
L82	30.0	0.4	1.01	0.01	36.1	0.4	0.84	0.01
G83	24.3	0.3	1.12	0.02	28.5	0.3	0.91	0.01
I84	28.9	0.5	1.05	0.02	37.3	0.6	0.84	0.02
W85	28.4	0.4	1.07	0.01	35.7	0.4	0.85	0.01
G86	22.2	0.4	1.17	0.02	26.4	0.5	0.97	0.02
A87	20.5	0.2	1.17	0.01	25.7	0.2	1.00	0.01
S88	19.4	0.2	1.09	0.01	23.4	0.2	0.93	0.01
G89	19.9	0.2	1.14	0.01	23.9	0.2	1.01	0.01
K90	22.8	0.2	1.10	0.01	27.6	0.2	0.96	0.01
L91	23.4	0.4	1.15	0.02	28.1	0.5	0.95	0.03
I92	24.6	0.3	1.10	0.01	29.3	0.3	0.96	0.01
T95	18.3	0.6	1.20	0.04	22.9	0.9	1.10	0.07
A96	15.0	0.3	1.18	0.03	19.8	0.5	1.04	0.03
V97	20.9	0.4	1.13	0.02	27.2	0.6	0.98	0.03
W99	21.7	0.6	1.22	0.04	27.4	1.0	1.03	0.05
N100	22.6	0.4	1.15	0.02	28.1	0.6	0.94	0.03
A101	17.3	0.2	1.14	0.01	22.0	0.2	0.97	0.01
S102	16.8	0.1	1.13	0.01	nd	nd	nd	nd
S104	17.7	0.2	1.13	0.01	nd	nd	nd	nd
N105	24.3	0.4	1.13	0.02	30.1	0.5	0.93	0.02
S107	26.9	0.6	1.02	0.02	34.2	0.6	0.83	0.02
L108	21.1	0.6	1.09	0.04	26.8	0.8	0.91	0.04
Q109	37.7	1.2	0.98	0.03	43.3	1.0	0.75	0.02
Q110	33.9	1.0	1.00	0.02	43.7	0.9	0.77	0.02
I 111	nd	nd	nd	nd	39.0	1.1	0.82	0.03

[a] All ^{15}N relaxation data have been recorded at 40 °C on the same 0.5 mM ^{2}H^{15}N^{13}C uniformly enriched homotrimeric gp41$^{1-194}$ (50 mM sodium acetate, pH 4.0, 25 mM KCl and 330 mM (≈ 115 mg/ml) DPC) as used for the backbone assignment. R_2 rates were corrected for the off-resonance tilted field, using the relation $R_2 = R_{1\rho}/\sin^2\theta - R_1/\tan^2\theta$ with $\tan\theta = \omega_1/\Omega$, where $R_{1\rho}$ is the directly measured decay rate of the $T_{1\rho}$ experiment, ω_1 is the spin-lock RF field strength and Ω the offset from the ^{15}N carrier.

Table S4b. ^{15}N-{^{1}H} NOE values measured at 600 and 800 MHz as well as transverse ^{15}N CSA –dipolar cross-correlated relaxation rates η_{xy} for gp41$^{1\text{-}194}$.

	I/I_0	$\Delta\ I/I_0$	I/I_0	$\Delta\ I/I_0$	$\eta_{xy}[s^{-1}]$	$\Delta\ \eta_{xy}$ $[s^{-1}]$	$\eta_{xy}[s^{-1}]$	$\Delta\ \eta_{xy}$ $[s^{-1}]$
	600MHz		800MHz		600MHz		800MHz	
V2	-0.27	0.01	0.01	0.01	3.2	0.1	3.7	0.1
G3	0.03	0.01	0.27	0.01	3.6	0.1	4.8	0.1
I4	0.46	0.02	0.54	0.01	13.5	0.2	17.1	0.2
G5	0.59	0.03	0.68	0.02	14.4	0.4	20.2	0.4
L7	0.55	0.02	0.68	0.01	15.2	0.4	20.8	0.3
F8	0.56	0.02	0.62	0.01	17.7	0.4	21.8	0.4
L9	0.6	0.03	0.67	0.02	17.7	0.5	22.0	0.5
G10	0.62	0.03	0.67	0.02	15.7	0.5	21.2	0.5
F11	0.54	0.02	0.64	0.01	16.6	0.3	22.1	0.3
L12	0.61	0.02	0.68	0.02	17.6	0.5	20.8	0.5
G13	0.53	0.03	0.62	0.02	13.5	0.5	18.4	0.5
A14	0.5	0.02	0.59	0.01	14.2	0.3	18.2	0.3
A15	0.4	0.02	0.52	0.01	11.3	0.2	15.3	0.2
G16	0.33	0.02	0.48	0.01	9.6	0.2	12.5	0.2
T18	0.33	0.01	0.45	0.01	9.0	0.1	12.6	0.1
M19	0.34	0.02	0.48	0.01	10.8	0.2	13.4	0.2
G20	0.3	0.02	0.43	0.01	7.4	0.2	10.8	0.2
A21	0.31	0.01	0.45	0.01	9.2	0.2	12.5	0.1
A22	0.32	0.02	0.44	0.01	10.4	0.2	13.6	0.3
S23	0.33	0.02	0.47	0.01	11.0	0.3	14.7	0.3
M24	0.34	0.02	0.48	0.02	12.4	0.3	17.3	0.4
T25	0.37	0.02	0.53	0.02	14.4	0.4	19.1	0.4
T27	0.51	0.05	0.65	0.03	21.2	1.2	28.8	1.3
Q29	0.53	0.03	0.66	0.02	23.6	0.7	33.7	1.0
A30	0.56	0.06	0.72	0.04	22.0	1.5	27.8	1.7
R31	0.59	0.05	0.7	0.03	23.1	1.3	32.0	1.3
Q32	0.64	0.03	0.71	0.02	nd	nd	34.3	1.0
L34	0.61	0.03	0.69	0.02	25.7	0.9	34.9	1.1
G36	0.57	0.04	0.67	0.02	24.5	1.0	31.7	0.9
I37	0.61	0.05	0.7	0.04	25.1	1.5	30.7	1.6
V38	nd	nd	0.64	0.02	24.0	0.8	29.8	1.0
L44	nd	nd	0.62	0.04	nd	nd	nd	nd
R46	0.58	0.04	0.63	0.03	nd	nd	nd	nd
A47	0.67	0.06	0.66	0.04	nd	nd	nd	nd
I48	0.6	0.05	0.64	0.03	nd	nd	nd	nd
I62	0.68	0.08	0.71	0.04	31.4	2.3	36.3	2.9
L65	0.58	0.03	0.63	0.02	nd	nd	nd	nd
A67	nd	nd	0.57	0.02	nd	nd	nd	nd
R68	0.67	0.07	0.58	0.05	nd	nd	nd	nd

I69	nd	nd	0.67	0.02	nd	nd	nd	nd
L70	0.53	0.05	0.64	0.03	nd	nd	34.4	1.8
E73	0.65	0.08	0.67	0.04	26.2	2.8	35.2	2.9
L76	0.55	0.07	0.6	0.04	nd	nd	nd	nd
N78	0.46	0.01	0.52	0.01	nd	nd	nd	nd
Q79	0.55	0.03	0.63	0.02	27.5	1.0	33.8	1.3
Q80	0.53	0.03	0.6	0.02	nd	nd	34.8	2.0
L81	0.44	0.03	0.56	0.02	22.6	0.8	29.8	1.0
L82	0.49	0.03	0.56	0.02	21.0	0.6	26.3	0.7
G83	0.48	0.03	0.56	0.02	14.9	0.5	21.7	0.5
I84	nd	nd	nd	nd	nd	nd	nd	nd
W85	0.53	0.02	0.63	0.02	nd	nd	nd	nd
G86	0.36	0.03	0.5	0.03	13.2	0.5	17.2	0.6
A87	0.4	0.02	0.53	0.01	13.5	0.2	19.3	0.2
S88	0.31	0.02	0.42	0.01	13.2	0.4	18.5	0.3
G89	0.29	0.02	0.42	0.01	14.0	0.3	18.4	0.3
K90	0.35	0.02	0.47	0.01	16.2	0.3	21.4	0.3
L91	0.33	0.04	0.5	0.03	15.0	0.7	21.1	0.9
I92	0.31	0.02	0.43	0.02	17.5	0.5	21.6	0.6
T95	0.34	0.06	0.36	0.05	11.9	1.0	15.7	1.4
A96	0.21	0.04	0.4	0.04	9.4	0.6	13.0	0.8
V97	0.28	0.04	0.48	0.03	nd	nd	nd	nd
W99	0.46	0.05	0.52	0.05	nd	nd	nd	nd
N100	0.44	0.03	0.51	0.03	13.7	0.2	16.6	0.2
A101	0.36	0.02	0.47	0.01	12.3	0.3	15.9	0.2
S102	nd	nd	0.46	0.01	11.1	0.3	15.3	0.2
S104	nd	nd	0.49	0.01	9.9	0.2	13.0	0.2
N105	0.43	0.04	0.51	0.03	16.6	0.6	21.5	0.6
S107	0.48	0.04	0.56	0.02	19.1	0.9	26.0	0.8
L108	nd	nd	0.52	0.04	nd	nd	nd	nd
Q109	0.51	0.05	0.65	0.04	27.8	1.6	34.2	1.7
Q110	0.54	0.05	0.66	0.03	26.0	1.4	32.9	1.4
I111	nd	nd	0.66	0.04	nd	nd	nd	nd

7. References

[1] P. Zhu, J. Liu, J. Bess, E. Chertova, J. D. Lifson, H. Grise, G. A. Ofek, K. A. Taylor, K. H. Roux, *Nature* **2006**, *441*, 847.
[2] Q. Sattentau, J. Moore, *J. Exp. Med.* **1991**, *174*, 407.
[3] D. S. Dimitrov, R. Blumenthal, *J. Virol.* **1994**, *68*, 1956.
[4] J. Munch, L. Standker, K. Adermann, A. Schuz, M. Schindler, R. Chinnadurai, S. Pohlmann, C. Chaipan, T. Biet, T. Peters, B. Meyer, D. Wilhelm, H. Lu, W. G. Jing, S. B. Jiang, W. G. Forssmann, F. Kirchhoff, *Cell* **2007**, *129*, 263.
[5] D. C. Douek, P. D. Kwong, G. J. Nabell, *Cell* **2006**, *124*, 677.
[6] S. C. Harrison, *Nat. Struct. Mol. Biol.* **2008**, *15*, 690.
[7] S. C. Harrison, in *Virus Structure and Assembly, Vol. 64*, **2005**, pp. 231.
[8] D. C. Chan, P. S. Kim, *Cell* **1998**, *93*, 681.

[9] W. Weissenhorn, A. Dessen, S. C. Harrison, J. J. Skehel, D. C. Wiley, *Nature* **1997**, *387*, 426.
[10] K. H. Roux, K. A. Taylor, *Curr. Opin. Struct. Biol.* **2007**, *17*, 244.
[11] I. A. Wilson, J. J. Skehel, D. C. Wiley, *Nature* **1981**, *289*, 366.
[12] J. J. Skehel, D. C. Wiley, *Annu. Rev. Biochem.* **2000**, *69*, 531.
[13] C. P. Jaroniec, J. D. Kaufman, S. J. Stahl, M. Viard, R. Blumenthal, P. T. Wingfield, A. Bax, *Biochemistry* **2005**, *44*, 16167.
[14] Y. L. Li, L. K. Tamm, *Biophys. J.* **2007**, *93*, 876.
[15] W. Qiang, Y. Sun, D. P. Weliky, *Proc. Natl. Acad. Sci. U. S. A.* **2009**, *106*, 15314.
[16] Z. Y. J. Sun, K. J. Oh, M. Y. Kim, J. Yu, V. Brusic, L. K. Song, Z. S. Qiao, J. H. Wang, G. Wagner, E. L. Reinherz, *Immunity* **2008**, *28*, 52.
[17] M. Kim, Z. Y. J. Sun, K. D. Rand, X. M. Shi, L. K. Song, Y. X. Cheng, A. F. Fahmy, S. Majumdar, G. Ofek, Y. P. Yang, P. D. Kwong, J. H. Wang, J. R. Engen, G. Wagner, E. L. Reinherz, *Nat. Struct. Mol. Biol.* **2011**, *18*, 1235.
[18] A. L. Lai, A. E. Moorthy, Y. L. Li, L. K. Tamm, *J. Mol. Biol.* **2012**, *418*, 3.
[19] N. A. Lakomek, J. F. Ying, A. Bax, *J. Biomol. NMR.* **2012**, *53*, 209.
[20] M. Caffrey, J. Kaufman, S. J. Stahl, P. T. Wingfield, A. M. Gronenborn, G. M. Clore, *J. Magn. Reson.* **1998**, *135*, 368.
[21] M. Lu, S. C. Blacklow, P. S. Kim, *Nature Structural Biology* **1995**, *2*, 1075.
[22] D. C. Chan, D. Fass, J. M. Berger, P. S. Kim, *Cell* **1997**, *89*, 263.
[23] V. Buzon, G. Natrajan, D. Schibli, F. Campelo, M. M. Kozlov, W. Weissenhorn, *PLoS Pathog.* **2010**, *6*, 7.
[24] G. M. Clore, A. Szabo, A. Bax, L. E. Kay, P. C. Driscoll, A. M. Gronenborn, *J. Am. Chem. Soc.* **1990**, *112*, 4989.
[25] D. M. Korzhnev, V. Y. Orekhov, A. S. Arseniev, *J. Magn. Reson.* **1997**, *127*, 184.
[26] G. Lipari, A. Szabo, *J. Am. Chem. Soc.* **1982**, *104*, 4546.
[27] R. Blumenthal, S. Durell, M. Viard, *J. Biol. Chem.* **2012**, *287*, 40841.
[28] G. Frey, S. Rits-Volloch, X. Q. Zhang, R. T. Schooley, B. Chen, S. C. Harrison, *Proc. Natl. Acad. Sci. U. S. A.* **2006**, *103*, 13938.
[29] Y. Kozlovsky, M. M. Kozlov, *Biophys. J.* **2002**, *82*, 882.
[30] D. Lee, C. Hilty, G. Wider, K. Wuthrich, *J. Magn. Reson.* **2006**, *178*, 72.
[31] F. Delaglio, S. Grzesiek, G. W. Vuister, G. Zhu, J. Pfeifer, A. Bax, *J. Biomol. NMR* **1995**, *6*, 277.
[32] A. S. Maltsev, J. F. Ying, A. Bax, *J. Biomol. NMR.* **2012**, *in press*.
[33] T. Yamazaki, A. P. Hinck, Y. X. Wang, L. K. Nicholson, D. A. Torchia, P. Wingfield, S. J. Stahl, J. D. Kaufman, C. H. Chang, P. J. Domaille, P. Y. S. Lam, *Protein Sci.* **1996**, *5*, 495.
[34] D. Noy, J. R. Calhoun, J. D. Lear, *Anal. Biochem.* **2003**, *320*, 185.
[35] P. T. Wingfield, S. J. Stahl, J. Kaufman, A. Zlotnick, C. C. Hyde, A. M. Gronenborn, G. M. Clore, *Protein Sci.* **1997**, *6*, 1653.
[36] S. W. Provencher, J. Glockner, *Biochemistry* **1981**, *20*, 33.
[37] D. I. Svergun, *J. Appl. Crystallogr.* **1992**, *25*, 495.
[38] D. I. Svergun, *Biophys. J.* **1999**, *76*, 2879.
[39] Y. Shen, A. Bax, *J. Biomol. NMR* **2010**, *48*, 13.
[40] Y. Shen, F. Delaglio, G. Cornilescu, A. Bax, *J. Biomol. NMR* **2009**, *44*, 213.
[41] Y. J. Wang, O. Jardetzky, *J. Am. Chem. Soc.* **2002**, *124*, 14075.
[42] J. P. Loria, M. Rance, A. G. Palmer, *J. Biomol. NMR* **1999**, *15*, 151.
[43] J. Iwahara, C. Tang, G. M. Clore, *J. Magn. Reson.* **2007**, *184*, 185.
[44] N. J. Anthis, M. Doucleff, G. M. Clore, *J. Am. Chem. Soc.* **2011**, *133*, 18966.
[45] J. J. Chou, S. Gaemers, B. Howder, J. M. Louis, A. Bax, *J. Biomol. NMR* **2001**, *21*, 377.
[46] N. C. Fitzkee, A. Bax, *J. Biomol. NMR* **2010**, *48*, 65.
[47] T. Yamazaki, W. Lee, C. H. Arrowsmith, D. R. Muhandirm, L. E. Kay, *J. Am. Chem. Soc.* **1994**, *116*, 11655.
[48] M. Salzmann, G. Wider, K. Pervushin, H. Senn, K. Wuthrich, *J. Am. Chem. Soc.* **1999**, *121*, 844.
[49] M. Ikura, A. Bax, G. M. Clore, A. M. Gronenborn, *J. Am. Chem. Soc.* **1990**, *112*, 9020.
[50] J. Weigelt, *Journal of American Chemical Society* **1998**, *120*, 10778.
[51] J. F. Ying, J. H. Chill, J. M. Louis, A. Bax, *J. Biomol. NMR* **2007**, *37*, 195.
[52] H. Geen, R. Freeman, *J. Magn. Reson.* **1991**, *93*, 93.
[53] K. V. Pervushin, G. Wider, K. Wuthrich, *J. Biomol. NMR* **1998**, *12*, 345.
[54] L. E. Kay, P. Keifer, T. Saarinen, *J. Am. Chem. Soc.* **1992**, *114*, 10663.
[55] L. Yao, B. Voegeli, J. F. Ying, A. Bax, *J. Am. Chem. Soc.* **2008**, *130*, 16518.
[56] L. Yao, A. Grishaev, G. Cornilescu, A. Bax, *J. Am. Chem. Soc.*, **2010**, *132*, 4295.
[57] D. M. Korzhnev, M. Billeter, A. S. Arseniev, V. Y. Orekhov, *Prog. Nucl. Magn. Reson. Spectrosc.* **2001**, *38*, 197.
[58] J. M. Schurr, H. P. Babcock, B. S. Fujimoto, *Journal of Magnetic Resonance Series B* **1994**, *105*, 211.